The impact of atmospheric motions on source-specific black carbon and the induced direct radiative effects over a river-valley region

Huikun Liu[1], Qiyuan Wang[1,2,3*], Suixin Liu[1,5], Bianhong Zhou[4], Yao Qu[1], Jie Tian[1], Ting Zhang[1], Yongming Han[1,2,3], Junji Cao[6,1,5*]

[1]Key Laboratory of Aerosol Chemistry and Physics, State Key Laboratory of Loess and Quaternary Geology, Institute of Earth Environment, Chinese Academy of Sciences, Xi'an, 710061, China
[2]CAS Center for Excellence in Quaternary Science and Global Change, Xi'an, 710061, China
[3]Guanzhong Plain Ecological Environment Change and Comprehensive Treatment National Observation and Research Station, Xi'an 710061, China
[4]Shaanxi Key Laboratory of Disaster Monitoring and Mechanism Simulation, College of Geography & Environment, Baoji University of Arts & Sciences, Baoji 721013, China
[5]Shaanxi Key Laboratory of Atmospheric and Haze-fog Pollution Prevention, Xi'an 710061, China
[6]Institute of Atmospheric Physics, Chinese Academy of Sciences, Beijing 100029, China

[*]*Correspondence to*: Qiyuan Wang (wangqy@ieecas.cn) and Junji Cao (jjcao@mail.iap.ac.cn)

Abstract. Black carbon (BC) is one of the most important short lived climate forcers, and atmospheric motions play an important role in determining its mass concentrations of pollutants. Here an intensive observation was launched in a typical river-valley city to investigate relationships between atmospheric motions and BC aerosols. Equivalent BC (eBC) source apportionment was based on an aethalometer model with the site-dependent absorption Ångström exponents (AAEs) and the mass absorption cross-sections (MACs) retrieved using a positive matrix factorization (PMF) model based on observed chemical components (i.e., EC, POC, K^+, Mg, Al, Si, S, Cl, Ca, V, Mn, Fe, Ni, Cu, As, Se, Br, Sr, Pb, Ga, and Zn) and primary absorption coefficients at selected wavelengths from λ = 370 to 880nm. The derived AAEs from 370 to 880nm were 1.07 for diesel vehicular emissions, 2.13 for biomass burning, 1.74 for coal combustion, and 1.78 for mineral dust. The mean values for eBC_{fossil} and $eBC_{biomass}$ were 2.46 μg $m^{-3}$and 1.17 μg m^{-3} respectively. Wind run distances and the vector displacements of the wind in 24 h were used to construct a self-organizing map, from which four atmospheric motions categories were identified (local-scale dominant, local-scale strong and regional-scale weak, local-scale weak and regional-scale strong and regional-scale dominant). BC pollution was found to be more likely when the influence of local-scale motions outweighed those of regional-scale motions. Cluster analysis for the back trajectories of air mass calculated by Hybrid Single-Particle Lagrangian Integrated Trajectory model at the study site indicated that the directions of air flow can have different impacts for different scales of motion. The direct radiative effects (DRE) of source-specific eBCs were lower when the influence of regional-scale motions outweighed that of the local ones. However, due to chemical aging of the particles during transport—the DRE efficiencies under regional scale motions were ~1.5 times higher than those under more local influences. The finding that the DRE efficiency of BC increased during the regional transport suggested significant consequences in regions downwind of pollution sources and emphasizes the importance of regionally transported BC for potential climatic effects.

1 Introduction

Black carbon (BC) is produced by the incomplete combustion of biomass and fossil fuels. The BC aerosol has a strong light absorption capacity and can cause heating of the atmosphere. In fact, BC is widely recognized as one of the most important short-lived climate forcers (IPCC, 2021). Due to this high light-absorbing ability, BC has the potential to perturb the radiative balance between the earth and atmosphere and in so doing cause in the climate to change and drive ecosystems away from their natural states (Schroter et all., 2005). Those changes ultimately will affect biodiversity and could threaten humans' food security (Ochoa-Hueso et al., 2017; Shindell et al., 2012). Besides heating the atmosphere directly, BC also is important for nucleating clouds, and that is another way in which the particles can cause indirect climatic effects (Jacobson, 2002). As BC is heterogeneously distributed in the atmosphere, its climatic effects are highly variable and dependent on its distribution in the atmosphere, both horizontally and vertically; its radiative properties and how they are affected by of chemical processing; and its lifetime (IPCC, 2021).

The radiative efficiency of BC can vary due to differences in emission sources and atmospheric aging processes (Bond et al., 2013; He et al., 2015; Cappa et al., 2012). Indeed, BC from different sources can vary in light absorbing abilities (Cheng et al., 2011) which can affect the radiative forcing of climate. In addition to the effects of the sources, regional transport can impact the light-absorbing ability through chemical processing or aging (Zhang et al., 2019). After BC particles are emitted, they can stay in the atmosphere for days or a few weeks (IPCC, 2021). During transport, fresh BC can experience a series of physical and chemical changes, for instance, mixing with other substances that can alter its microphysical and optical properties (Kahnert and Kanngießer, 2020). The aging processes can be even faster in polluted regions (Peng et al., 2016), and as a result, the light-absorbing ability of BC can be strongly affected. Indeed, the light absorption ability of BC after aging can be as much as 2.4 times that of fresh particles (Peng et al., 2016).

The concentrations of BC are controlled by local emissions and regional transport, but meteorological conditions also are important because they affect both transport and removal. Normally, local emissions in urban areas are predictable to some degree because those emission sources are mainly anthropogenic and the concentrations of pollutants follow the diurnal patterns driven by anthropogenic activities. By contrast, meteorological conditions and regional transport are governed by multiple scales of motion which result in distinct meteorological impacts on ambient pollutant levels (Levy et al., 2010, Dutton, 1976). A commonly accepted classification of the scale of motion is based on horizontal distance and time scales. Typically, the time scale of local-scale motions varies from hours to days and the spatial scale ranges from 10^2 to 10^5 m (Oke et al., 2002; Seinfeld and Pandis, 2006). The local scales of motion are mainly controlled by local factors such as the roughness of the earth's surface, orography, land breeze/sea breeze circulation, etc. (Hewitson and Crane, 2006; IPCC, 2021). Larger scale of motions are associated with a mesoscale or synoptic scale weather systems, which on the one hand can transport pollutants but on the other can disperse them (Kalthoff et al., 2000; Zhang et al., 2012).

The relationships between atmospheric motions and pollutant concentrations are complex. Atmospheric motions determine where and how extensive the pollution impacts are, but of course the rates of pollutant emissions, especially local ones, are important, too (Dutton, 1976). Liao et al., (2020) found that synoptic-scale flow led to an enhanced $PM_{2.5}$ in a coastal area of the Pearl River Delta, while meso/local scale motions led to $PM_{2.5}$ pollution in an inland area. Levy et al. (2010) showed that the concentrations of NO_x and SO_2 were higher under the dominance of smaller-scale motions than under larger scale motions.

However, few studies have touched on the impacts of different scales of motion on BC and their effects on radiative efficiency even though the effects could cause rapid climatic effects due to the patchy and constantly changing distributions (IPCC, 2021).

Topography also plays an important role in air pollution (Zhao et al., 2015). River-valley topography is complicated, and it can have a considerable influence on air pollution and synoptic patterns of flow (Green et al., 2016; Carvalho et al., 2006). The pollution levels at cities in river-valleys are not only influenced by general atmospheric dynamics but also strongly impacted by the local-scale of dynamics (Brulfert et al., 2006). Surface albedo and surface roughness are affected by the complex topography of river-valley regions, and those physical factors can affect circulation causing changes in pollutant mass concentrations (Wei et al., 2020). Mountains also significantly affect pollution, and once pollutants are generated or transported into the river-valley regions, their dispersal can be impeded by the blocking effect of the mountains. Instead of being dispersed, they can be carried by the airflows over the mountains to converge at the bottom of the valley and increase the pollutants along the river (Zhao et al., 2015). In this way, pollutants can accumulate in valleys and spread throughout the area, thereby aggravating pollution. In addition, temperature inversions commonly form in river-valleys during the winter, and that, too, can aggravate pollution problems (Glojek et al., 2022 and Bei et al., 2016).

Thus, we focused our study on the impacts of different scales of motion on source-specific equivalent BCs (eBCs), and we evaluated radiative effects of eBCs over a river-valley city. The primary objectives of this study were: (1) to quantify the contributions of fossil fuel combustion and biomass burning to eBC concentrations, (2) to investigate the impacts of different scales of motion on the source-specific eBC, and (3) to estimate the radiative effects and the radiative efficiency of the source-specific eBC under different atmospheric motion scenarios. The study provides insights into the influence of the specified atmospheric motions on BC and highlights the effects of those motions on the radiative efficiency and potential climatic effects of the regionally transported BC.

2 Methodology

2.1 Research site

Baoji is a typical river-valley city, located at the furthest west of the Guanzhong Plain, at an altitude from 450 to 800 m a.s.l. (Figure S1), Baoji has a complex topography and often suffering from severe pollution in winter. It is surrounded by mountains to the south, west and north, with the Weihe River as the central axis extending eastward. The shape can be viewed as a funnel, with large opening to east. The Qinling peaks and the flat Weihe Plain are the main landforms of Baoji. The main peak of the Qinling Mountains is 3,767 m a.s.l. and it is the highest mountain in the eastern part of mainland China. This terrain causes divergent flow at local scales, which can impact pollution levels (Wei et al., 2020). Baoji also is an important railway intersection in China, connecting six railways to the north-west and southwest China. Pollutant levels can be high and pollutants are not easy to be dispersed in the city due to its special topographic conditions, dense population (total population of 0.341 million, with 63.5% population living in the downtown aera and population density of 6003 people per km^2 in 2019 (http://tjj.shaanxi.gov.cn/upload/2021/zk/indexch.htm and https://data.chinabaogao.com/hgshj/2021/042053X932021.html), and impacts from major highway and railway networks.

The sampling site was on the rooftop of a building at Baoji University of Arts and Sciences (34°21′16.8″N, 107°12′59.6″E, 569 m a.s.l.) surrounded by commercial and residential buildings, highways, and a river, there were no major industrial emission sources nearby. The main sources of BC in Baoji were the domestic fuel (coal and biomass) burning as well as the motor vehicle emissions (Zhou et al., 2018; Xiao et al., 2014). Open fire also can be sources for BC, but there were limited fire found scattered around the site (Figure S2). The meteorological conditions at Baoji for the four seasons are listed in Table S1, and the wind roses for the different seasons are shown in Figure S3(data are from the Meteorological Institute of Shaanxi Province).

2.2 Sampling and laboratory measurements

eBC and the absorption coefficients (b_{abs}) at 370, 470, 520, 590, 660, 880, and 950 nm wavelength were measured using an AE33 aethalometer (Magee Scientific, Berkeley, CA, USA) equipped with a $PM_{2.5}$ cut-off inlet (SCC 1.829, BGI Inc. USA) that had a time resolution of 1 min. A Nafion® dryer (MD-700-24S-3; Perma Pure, Inc., Lakewood, NJ, USA) with a flow rate of 5 L min^{-1} was used to dry the $PM_{2.5}$ before the measurement. Briefly, the particles were dried by the Nafion® dryer before being measured with the AE33 aethalometer, and the deposited particles were irradiated by light-emitting diodes at seven wavelengths (λ = 370, 470, 520, 590,660, 880, and 950 nm), and the light attenuation was detected. The non-linear loading issue for filter-based absorption measurement was accounted for in the AE33 by a technique called dual-spot compensation. The quartz filter (PN8060) matrix scattering effect was corrected by using a factor of 1.39. More details of AE33 measurement techniques can be found in Drinovec et al. (2015).

The scattering coefficient (b_{scat}) at a single (525) nm wavelength was measured with the use of a nephelometer (Aurora-1000, Ecotech, USA) that had a time resolution of 5 min. The nephelometer and aethalometer operated simultaneously and used the same $PM_{2.5}$ cyclone and Nafion® dryer. The calibration was conducted based on the user guide with a calibration gas R-134. Zero calibrations were conducted every other day by using clean air without particles. The ambient air was drawn in through a heated inlet with a flow rate of 5 L min^{-1}. The relative humidity remained lower than 60%.

$PM_{2.5}$ samples were collected for every 24 hours (h) from 10 a.m. local time to the 10 a.m. the next day from 16th November 2018 to 21st December 2018 with two sets of mini-volume samplers (Airmetrics, USA), one using quartz fiber filters (QM/A; Whatman, Middlesex, UK) and the other with Teflon® filters (Pall Corporation, USA), both with a flow rate of 5 L min^{-1}. The samples were kept in a refrigerator at 4°C before analysis. The mass concentration of K^+ in the $PM_{2.5}$ quartz sample was extracted in a separate 15 mL vials containing 10 mL distilled deionized water (18.2 MΩ resistivity). The vials were placed in an ultrasonic water bath and shaken with a mechanical shaker for 1 h to extract the ions, which and determined by a Metrohm 940 Professional IC Vario (Metrohm AG., Herisau, Switzerland) with Metrosep C6-150/4.0 column (1.7 mmol/L nitric acid+1.7 mmol/L dipicolinic acid as the eluent) for cation analysis. A group of elements (i.e. Mg, Al, Si, S, Cl, Ca, V, Mn, Fe, Ni, Cu, As, Se, Br, Sr, Pb, Ga, and Zn) on the Teflon® filters was were determined by energy-dispersive x-ray fluorescence (ED-XRF) spectrometry (Epsilon 4 ED-XRF, PANalytical B.V., Netherlands). The X-rays were generated from a gadolinium anode on a side-window X-ray tube. A spectrum of the ratio of X-ray and photon energy was obtained after 24 minutes of analysis for each sample with each energy peak characteristic of a specific element, and the peak areas were proportional to the concentrations of the elements. Quality control was conducted on a daily basis with a test standard sample.

Organic carbon (OC) and elemental carbon (EC) in each sample were determined with the use of a DRI Model 2001 Thermal/Optical Carbon Analyzer (Atmoslytic Inc., Calabasas, CA, USA). The thermal/optical reflectance (TOR) method and IMPROVE_A protocol were used for analysis. A punch of a quartz filter sample was heated at specific temperatures to obtain data for four OC fractions and three EC fractions. Total OC was calculated by summing all OC fractions and the pyrolytic carbon (PC). Total EC was calculated by summing all EC fractions minus the PC. Detailed methods and quality assurance/quality control processes were described in Cao et al., (2003). Primary organic carbon (POC) was estimated by using the minimum R-squared (MRS) method, which is based on using eBC as a tracer (Text S1). The method uses the minimum R^2 between OC and eBC to indicate the ratio for which secondary OC and eBC are independent. A detailed description of the MRS method can be found in Wu et al., (2016).

Concentration of NO_x, wind speed, and direction at 12 ground monitoring sites were downloaded from http://sthjt.shaanxi.gov.cn/hx_html/zdjkqy/index.html. The wind data at 100 meters (m) above the ground and the planetary boundary layer height were downloaded from https://rda.ucar.edu/datasets/ds633.0. The data used for the Hybrid Single-Particle Lagrangian Integrated Trajectory (HYSPLIT) model was downloaded from Global Data Assimilation System and it had a resolution of 1°×1° (GDAS, https://www.ready.noaa.gov/gdas1.php). The data and main parameters used in trajectory model are listed in Table S2.

2.3 Optical source apportionment

The positive matrix factorization (PMF) model that was used for the optical source apportionment in this study. PMF solves chemical mass balance by decomposing the observational data into different source profiles and contribution matrices as follows:

$$X_{ij} = \sum_{k=1}^{p} g_{ik} f_{kj} + e_{ij} \quad (1)$$

where X_{ij} denotes the input data matrix; p is the number of sources selected in the model; g_{ik} denotes the contribution of the k^{th} factor to the i^{th} input data; f_{kj} represents the k^{th} factor's profile of the j^{th} species; and e_{ij} represents the residual. Both g_{ik} and f_{kj} are non-negative. The uncertainties of each species and $b_{abs}(\lambda)$ were calculated by the equation recommended in EPA PMF5.0 user guideline(Norris et al, 2014) as follows:

$$Unc = \sqrt{(error\ fraction \times concentration(or\ ligth\ absorption\ coefficient))^2 + (0.5 \times MDL)^2} \quad (2)$$

$$Unc = \frac{5}{6} \times MDL \quad (3)$$

where MDL is the minimum detection limit of the method. When the concentration of a species was higher than the MDL then equation (2) was used otherwise equation (3) was used. In equation (2), for calculating the uncertainty of a chemical species, the error fraction was multiplied the concentration of the species. For calculating the uncertainty of optical data, the error fractions were multiplied by the light absorption coefficients.

Chemical species data (EC, POC, K^+, Mg, Al, Si, S, Cl, Ca, V, Mn, Fe, Ni, Cu, As, Se, Br, Sr, Pb, Ga and Zn) and the primary absorption coefficients (Pabs) data at λ=370nm,470nm,520nm,660nm, and 880nm were used for PMF analysis. The error fraction of offline measured data was the difference between multiple measurements of the same sample. The error fraction

used for optical data was 10% based on Rajesh and Ramachandran (2018). PMF solves the equation (1) by minimizing the Q value, which is the sum of the normalized residuals' squares, as follows,

$$Q = \sum_{i=1}^{n} \sum_{j=0}^{n} \left[\frac{e_{ij}}{u_{ij}}\right]^2 \quad (4)$$

where u_{ij} represents the uncertainties of each X_{ij} and Q_{true}/Q_{exp} was used as the indicators for the factor number determination.

2.4 eBC source apportionment

The quantities of eBC generated from biomass burning versus fossil fuel combustion were deconvolved by an aethalometer model which uses Beer-Lambert's Law to write the absorption coefficients equations, wavelengths and absorption Ångström exponents (AAEs) for the two different BC emission sources (Sandradewi et. al., 2008). This approach is widely used for separating BC from two different sources based on optical data (Rajesh et al., 2018; Kant et al., 2019; Panicker et al., 2010). However, the traditional aethalometer model could be affected by the light absorbing substances at lower wavelengths such as dust and secondary aerosol. An improvement to the traditional aethalometer model was made, by explicitly considering the interference of the b_{abs} at a lower wavelength (370nm) caused by dust and secondary OC. Thus, the calculation of the absorption and source apportionment was based on the following equations (Wang et al., 2020):

$$\frac{b_{abs}(370)_{fossil}}{b_{abs}(880)_{fossil}} = \left(\frac{370}{880}\right)^{-AAE_{fossil}} \quad (5)$$

$$\frac{b_{abs}(370)_{biomass}}{b_{abs}(880)_{biomass}} = \left(\frac{370}{880}\right)^{-AAE_{biomass}} \quad (6)$$

$$b_{abs}(880) = b_{abs}(880)_{fossil} + b_{abs}(880)_{biomass} \quad (7)$$

$$b_{abs}(370) = b_{abs}(370)_{fossil} + b_{abs}(370)_{biomass} + b_{abs}(370)_{secondary} + b_{abs}(370)_{dust} \quad (8)$$

$$eBC_{fossil} = \frac{b_{abs}(880)_{fossil}}{MAC_{BC}(880)_{fossil}} \quad (9)$$

$$eBC_{biomass} = \frac{b_{abs}(880)_{biomass}}{MAC_{BC}(880)_{biomass}} \quad (10)$$

where AAE_{fossil} and $AAE_{biomass}$ are the AAEs for fossil fuel combustion and biomass burning. These were derived from the optical source apportionment by using PMF as discussed in section 3.1. Further, $b_{abs}(370)$ and $b_{abs}(880)$ are the total b_{abs} measured by the AE33 at the wavelengths of 370 nm and 880 nm respectively; $b_{abs}(370)_{fossil}$ and $b_{abs}(880)_{fossil}$ are the b_{abs} caused by emissions from fossil fuel combustion at those two wavelengths; $b_{abs}(370)_{biomass}$ and $b_{abs}(880)_{biomass}$ are the b_{abs} caused by emissions from biomass burning at those two wavelengths; $b_{abs}(370)_{dust}$ refers to the b_{abs} contributed by mineral dust at the wavelength of 370 nm, which was derived from the result of optical source apportionment; $b_{abs}(370)_{secondary}$ refers to the b_{abs} caused by the secondary aerosols at the wavelength of 370 nm, which was calculated by the minimum R-squared approach with eBC as a tracer (Text S1, Wang et al., 2019); eBC_{fossil} and $eBC_{biomass}$ are the eBCs from fossil fuel combustion and biomass burning; and $MAC_{BC}(880)_{fossil}$ and $MAC_{BC}(880)_{biomass}$ are the mass absorption cross-sections of eBC_{fossil} and the mass absorption cross-section of $eBC_{biomass}$ at the wavelength of 880 nm respectively, which were based on the PMF results for the optical source apportionments.

2.5 Indicators for the different scales of motion

The mathematical definitions of airflow condition proposed by Allwine and Whiteman (1994) were used in this study. The definitions quantify the flow features integrally at individual stations. Three variables were quantified, namely the actual wind run distance (*S*) which is the scalar displacement of the wind in 24 h (i.e. the accumulated distance of the wind), the resultant transport distance (*L*) which is the vector displacement of the wind in 24 h (i.e. the straight line from the starting point to the end point), and the recirculation factor (*R*) is based on the ratio of *L* and *S* which indicates the frequency of the wind veering in 24 h. The influences of different scales of atmospheric motions were assessed based on the method proposed by Levy et al., (2010), and for this, we used wind data at 100 m above the sampling site and the wind data from 12 monitoring stations at ground level (~15m) to indicate the different scales of motions. The winds at the surface monitoring stations were expected to be more sensitive to local-scale turbulence and convection than the winds at 100 m. With less influence from the surface forces, the indicators at 100 m would be more sensitive to larger scales of motion. The equations used as follows:

$$L_{n\tau/bj} = T\left[\left(\sum_{j=i}^{i-\tau+1} u_i\right)^2 + \left(\sum_{j=i}^{i-\tau+1} v_i\right)^2\right]^{1/2} \quad (11)$$

$$S_{n\tau/bj} = \sum_{j=i}^{i-\tau+1}(u_j{}^2 + v_j{}^2)^{1/2} \quad (12)$$

$$R_{n\tau/bj} = 1 - \frac{L_{i\tau}}{S_{i\tau}} \quad (13)$$

where T is the interval of the data (i.e., 60 min), i is the i^{th} the ending time step data, τ is the integration time period of the wind run (24 h), i-τ+1 represents the data at the start time, and n is the number of monitoring stations (a total of 12 in this study). The quantities u and v are the wind vectors. Using the wind data from the 12 monitoring stations covering Baoji, the *L* and *S* values at the 12 different sites at ground level were calculated. $L_{n\tau}$ and $S_{n\tau}$ represent the resultant transport distance and the actual wind run distance at the n^{th} (n = 1 to 12) monitoring station at ground level; $R_{n\tau}$ is the recirculation factor at the n^{th} monitoring station which is calculated based on $L_{n\tau}$ and $S_{n\tau}$; $L_{bj,}$ and S_{bj} are the resultant transport distance and the actual wind run distance at 100 m height above the ground. These represent the flow characteristics in higher atmosphere at the study site, and they were calculated by using the wind data at 100 m height. The recirculation factor (R_{bj}) was calculated for a height of 100 m.

As explained in Levy et al., (2010), if local-scale motions are strong and regional-scale motions are weak, the variations in winds at each station would not be likely to be uniform due to differences in local factors, and that would result in relatively large standard deviations (R_{std}) for $R_{n\tau}$. By contrast, if the local-scale motions are weak and the regional-scale motions are strong, the wind direction would be likely to be more uniform over a large area, and the R_{bj} and the R_{std} should be relatively smaller.

2.6 Self-organizing map

A self-organizing map (SOM) developed by Kohonen (1990) is a type of artificial neural network that is widely used for categorizing high-dimensional data into a few major features (Stauffer et al., 2016 and Pearce et al., 2014). In particular, this approach is widely used for categorizing different meteorological patterns (Liao et al., 2020; Han et al., 2020; Jiang et al., 2017). Unlike traditional dimension reduction methods (e.g., principal component analysis), SOM projects high-dimensional

input data by non-linear projection into user-designed lower-dimensions, which are typically two-dimensional arrays of nodes (Hewitson and Crane, 2006). The performance of SOM in classifying climatological data has been shown to be robust (Reusch et al., 2005). Competitive learning algorithms are used to train SOM, and the architecture of SOM consists of two layers; one is called the input layer and it contains the high dimensional input data. The other layer is the output layer in which the node number is the output cluster number. The working principle of SOM is to convert high dimensional data with complex correlations into lower dimensions via geometrical relationships (Ramachandran et al., 2019). After the initial random weights are generated, the input data are compared with each weight, and the best match is defined as winning. The winning node and the neighboring nodes close to the winning node will learn from the same inputs and the associated weights are updated. After multiple iterations, the network to settles into stable zones of features and the weights. More detailed working principles of SOM can be found Kangas and Kohonen, (1996) and Kohonen et al., (1996).

Comparison between the input data and each weight is made by applying Euclidean distances, the best match is defined by the following equation:

$$\|x - m_c\| = min\{\|x - m_i\|\} \quad (14)$$

where x is the input data, $m_c$is the best matched weight, $m_i$is the weights connected with the i^{th} node.

The weights are updated by following equation:

$$m_i(t+1) = m_i(t) + h_{ci}(t)[x(t) - m_i(t)] \quad (15)$$

where the $m_i(t+1)$ is the i^{th} weight at t+1 time, $m_i(t)$is the i^{th} weight at t time, the $h_{ci}(t)$ is the neighborhood kernel defined over the lattice points at t time, and c is the winning node location.

SOM was used to categorize the daily atmospheric motions during the study period and to explore the influences of different scales of motion on source-specific eBC. Hourly averages of three sets of data (R_{std}, L_{bj}, and S_{bj}) were input into SOM. Determining the size of the output map is crucial for SOM (Chang et al 2020 and Liu et al., 2021). To reduce the subjectivity, the K-means cluster method was used for the decision-making regarding size. The similarity of each item of the input data relative to the node was measured using Euclidean distance. The iteration number was set to 2000. For each input data item, the node closest to it would "win out". The reference vectors of the winning node and their neighborhood nodes were updated and adjusted towards the data. The "Kohonen" package in *R* language (Wehrens and Kruisselbrink, 2019) was used to develop the SOM model in this study.

2.7 Estimations of direct radiative effects and heating rate

The Santa Barbara DISORT Atmospheric Radiative Transfer (SBDART) model was used to estimate the direct radiative effects (DRE) induced by source-specific eBC. The model has been used in many studies to calculate the DRE caused by aerosols and BC (Pathak et al., 2010; Rajesh et al., 2018; Zhao et al., 2019). SBDART calculated DRE based on several well-tested physical models. Details regarding the model were presented in Ricchiazzi et al., (1998). The important input data included aerosol

parameters, including aerosol optical depth (AOD), single scattering albedo (SSA), asymmetric factor (AF) and extinction efficiency, surface albedo, and atmospheric profile.

The aerosol parameters used in this study were derived by the Optical Property of Aerosol and Cloud (OPAC) model (Hess et al., 1998) based on the number concentrations of aerosol components. As the study was conducted in an urban region, the urban aerosol profile was used in OPAC, and it included soot (eBC), water-soluble matter (WS), and water-insoluble matter (WIS). The number concentrations of soot were derived from the mass concentrations of eBC with the default ratio (5.99E-5 μg m^{-3}/ particle.cm^{-3}) in OPAC. The number concentrations of WS and WIS were adjusted until the modeled SSA and b_{abs} at 500nm in OPAC were close (±5%, see Figure S4) to those values calculated with data from the nephelometer and AE33 ($b_{ext}(520) = b_{scat}(525) + b_{abs}(520)$, SSA= $b_{scat}(525)/b_{ext}(520)$). The DRE of source-specific eBC at the top of atmosphere (TOA) and surface atmosphere (SUF) were calculated from the difference between the DREs with or without the number concentrations of the source-specific eBC under clear-sky conditions.

$$DRE_{eBC} = (F\downarrow - F\uparrow)_{with\ eBC} - (F\downarrow - F\uparrow)_{without\ eBC} \quad (16)$$

$$DRE_{eBC,ATM} = DRE_{eBC,TOA} - DRE_{eBC,SUF} \quad (17)$$

where DRE_{eBC} is the DRE of source-specific eBC, $F\downarrow$ and $F\uparrow$ are the downward and upward flux, $DRE_{eBC,ATM}$ is the DRE of the source-specific eBC for the atmospheric column, that is, the DRE at the top of the atmosphere ($DRE_{eBC,TOA}$) minus that at the surface ($DRE_{eBC,SUF}$).

3 Results and discussion

3.1 Calculation of eBC_{fossil} and $eBC_{biomass}$

The PMF model was used for the optical source apportionment, and those results were used to obtain the site-specific AAEs and MACs, which in turn were used to calculate the source-specific eBC with the improved aethalometer model. For every solution, PMF was run 20 times. The Q_{true}/Q_{exp} ratios from the 2- to 7-factor solutions were examined, and the values of a 4-factor solution were found most stable compared with others because the Q_{true}/Q_{exp} values did not drop appreciably after the addition of one more factor (Figure S5). Based on these results, the 4-factors solution was determined to be the most interpretable. Two diagnostic methods, Bootstrap (BS) and Displacement (DISP) (Norris et al, 2014; Brown et al. 2015) were used to validate the robustness and stability of the results. The BS method was used to assess the random errors and partially assess the effects of rotational ambiguity while DISP was used to evaluate rotational ambiguity errors. The results of the BS and DISP analyses showed that there was no swap for the 4-factor solution (Table S3). The modelled primary $b_{abs}(\lambda)$ were well correlated (r = 0.95–0.96, slope = 0.90~0.95, $p < 0.01$, Figure S6) with their observed counterparts, which suggested that the modelling performance of PMF5.0 was good. The factor profiles obtained from the PMF are shown in Figure 1.

The first factor (PC1) had was featured with high loadings of EC (52%), POC (49%), and V (49%) and moderate loadings of Mn (33%), Ni (40%), Cu (37%), and Zn (44%). This factor source contributed 27% to 44% of the primary $b_{abs}(\lambda)$. Of the species with high loadings on PC1, EC has been found to be associated with vehicular emissions due to incomplete fuel combustion (Cao et al., 2013). V and Ni are commonly detected in the particles emitted by diesel-powered vehicles (Lin et al., 2015 and

Zhao et al., 2021). Mn compounds are commonly used as an antiknock additive for unleaded gasoline to raise octane numbers and protect the engine (Lewis et al., 2003; Geivanidis et al., 2003); and Cu and Zn are emitted by the combustion of lubricating oils and from the wear of motor vehicle parts (i.e., brakes and tires) (Thorpe and Harrison, 2008; Song et al., 2006). In addition, the EC associated with this factor was found well correlated ($r = 0.83$, $p < 0.01$, Figure S7) with the daily averaged NO_x which is a commonly used tracer of vehicular emissions in the urban areas (Zotter et al., 2017). Recent research on the source contributions of BC emissions has shown that most of BC associated with transportation was emitted by on-road diesel vehicles in China (Xu et al., 2021). From these results, PC1 was identified as diesel vehicular emissions. The MAC of this factor ($MAC(880)_{diesel}$) was 6.7 $m^2\ g^{-1}$. The estimated AAE of this factor (AAE_{diesel}) was 1.07 (Figure S8), which is comparable with the AAE values of vehicle emissions (0.8~1.1) reported in previous studies (Zotter et al., 2017; Kirchstetter et al., 2004).

The second factor (PC2) was characterized by the high loadings of K^+ (51%), Cl (79%), and Br (52%) and moderate amounts of EC (26%), POC (28%), and Pb (30%). Of these, K^+ is a widely recognized tracers for the biomass burning emissions (Urban et al., 2012; Zhang et al., 2015), and high loadings of Cl also can be taken as a signal of biomass burning (Yao et al., 2002; Manousakas et al., 2017). Previous studies showed that a large quantity of Br was found in biomass burning aerosols was caused by emissions of CH_3Br emission during combustion (Manö and Andreae, 1994; Artaxo et al.,1998). Particulate matter emitted from biomass burning typically has substantial amounts of OC and EC (Song et al, 2006), and Pb also has been observed in biomass-burning aerosols (Amato et al., 2016). Thus, PC2 was identified as emissions from biomass burning. The contribution of this factor to primary $b_{abs}(370)$ was as high as 50%, but only 33% to primary $b_{abs}(880)$, and that was likely caused by the brown carbon which is a typically found in biomass-burning aerosols (Washenfelder et al., 2015; Yan et al., 2015). The MAC of this factor ($MAC(880)_{biomass}$) was 9.5 $m^2\ g^{-1}$. The AAE of this factor ($AAE_{biomass}$) was 2.13 (Figure S8), which is consistent with the wide range of AAEs reported for biomass-burning (1.2~3.5) (Sandradewi et al., 2008; Helin et al., 2018; Zotter et al., 2017).

The third factor (PC3) had significant loadings of S (64%), Se (98%), As (51%), and Pb (53%) and moderate loadings of Ga (42%)—all of these elements are commonly associated with coal combustion (Hsu et al., 2016; Tan et al., 2017). For instance, coal combustion has gradually become the main source of Pb in $PM_{2.5}$ after China began to phase out Pb-containing gasoline (Xu et al. 2012). Thus, PC3 was assigned to coal combustion. The MAC of this factor ($MAC(880)_{coal}$) was 7.5 $m^2\ g^{-1}$. This factor contributed 17%–19% primary $b_{abs}(\lambda)$, and its derived AAE_{coal} was 1.74 (Figure S8) which is close to the AAE found for coal-chunks (Sun et al., 2017).

The last factor (PC4) was most heavily loaded with Al (68%), Si (76%), Ca (65%), Fe (51%), and Sr (71%). These elements are typical crustal elements, and they are abundant in mineral dust (Tao et al., 2016; Tao et al., 2017). Minor amounts of EC in crustal dust could be from other EC that had deposited on the ground and later resuspended together with the dust by natural or artificial disturbances (e.g., wind and traffic flow). This factor only contributed ~4% of the primary $b_{abs}(\lambda)$. The estimated AAE_{dust} was 1.78 (Figure S8) which is close to the AAE of mineral dust reported in previous studies ($AAE_{370\sim950} = 1.82$, Yang et al., 2009).

As elaborated above, the $PM_{2.5}$ EC over Baoji was mainly from diesel vehicular emissions, biomass burning, and coal combustion. The emissions can be further grouped into those from biomass burning and fossil fuel combustion (the sum of diesel vehicular emissions and coal combustion). Thus, the AAE_{fossil} (1.26) and $MAC(880)_{fossil}$ (7.1 $m^2\ g^{-1}$) were calculated

was the mass-weighted averages (relative to the total EC) of AAE_{coal} ($MAC\ (880)_{coal}$) and AAE_{diesel} ($MAC\ (880)_{diesel}$) (Table S4). The hourly mass concentrations of eBC_{fossil} and $eBC_{biomass}$ were then calculated using the 'aethalometer model' (Eqs. 5–10). The results showed that eBC_{fossil} and $eBC_{biomass}$ were only weakly correlated (r = 0.3, Figure S9), indicating a reasonably good separation, and furthermore, their diel variations showed different patterns (Figure 2).

The mean values of eBC_{fossil} and $eBC_{biomass}$ were 2.46 μg m^{-3} and 1.17 μg m^{-3}, respectively. The averaged total eBC mass concentration (± standard deviation) was 3.63±2.73μg m^{-3}, and the eBC ranged from varying from 0.39 to 12.73 μg m^{-3} during the study period, The averaged mass concentration was comparable to that in Lanzhou, another river valley city in China, that was sampled in the same season (5.1 ± 2.1, Zhao et al.,2019). The lowest value is comparable to other river valley regions such as in Retje in India (Glojek et al., 2022) or in Urumqi River Valley in China (Zhang et al., 2020), however even the highest concentration was much lower than that in other urban regions (Table S5).

The diel variations of eBC_{fossil} (Figure 2a) showed a bimodal pattern with two peaks at 9 a.m. and 7 p.m local time. which are typical peak commuting hours, indicating that there were strong influences from traffic emissions. Due to the reduced traffic flow from 1 a.m. to 5 a.m., eBC_{fossil} decreased slowly. After 5 a.m. passenger vehicles were allowed on the highways in and near Baoji, and eBC_{fossil} started to rise, probably in response to the increased traffic emissions. As the morning commuter traffic increased, eBC_{fossil} reached its first peak at 9 a.m. From then until 11 a.m., eBC_{fossil} declined only slightly because the wind speeds decreased (Figure 2c), which offset the effects of the decreases in traffic. From 11 a.m. to 3 p.m., the increases in the height of the planetary boundary layer (PBLH) (Figure 2d) led to a rapid decrease in eBC_{fossil}. Later the PBLH decreased rapidly, resulting in conditions unfavorable for dispersion, and then eBC_{fossil} rose quickly to the second peak at 7 p.m. After passing the evening peak in traffic, the eBC_{fossil} decreased dramatically.

In contrast, the diel variation of $eBC_{biomass}$ (Figure 2b) showed greater influences from meteorological conditions during the daytime, and $eBC_{biomass}$ showed lower concentrations during the day compared with the night. After 6 p.m., increased biomass burning from cooking and residential heating let to the emission of more $eBC_{biomass}$ and the stable PBLH hindered the dispersion of $eBC_{biomass}$; these two factors caused the $eBC_{biomass}$ to reach its peak at 8 p.m. At night, the downslope winds from the mountains converged in the valley at night time (Oke et al., 2002) and turned easterly, where the land altitude is lower than at Baoji (Zhao et al., 2015). This led to t relatively strong winds (Figure 2c) favored dispersion and caused the measured $eBC_{biomass}$ pollutant levels to decrease.

3.2 The influence of regional and local atmospheric motion on eBC_{fossil} and $eBC_{biomass}$

The K-means results showed that the four-category solution was appropriate for interpretation as explained above (see also Figure S10). Thus a 2×2 map size was used for the self-organizing map (SOM). The four featured atmospheric motion categories given by SOM (Figure S11) were identified as follows (feature values are in Table 1):

1. Local-scale dominance (LD): This category featured high R_{bj} and R_{std}. As described in section 2.5, high R_{std} indicates greater divergence of R at the 12 stations due to the strong influence of local-scale turbulence and convection. L_{bj} and S_{bj} were shorter than 130 km implying stagnation (Allwine and Whiteman, 1994).

2. Local-scale strong and regional-scale weak (LSRW): For this group, L_{bj} and S_{bj} were longer than those for LD, and R_{std} was slightly lower than that in LD.

3. Local-scale weak and regional-scale strong (LWRS): As the values suggest, both R_{bj} and R_{std} were lower than those in LD and LSRW, especially R_{bj}. This suggests the winds veered less frequently and the differences of R found in 12 stations were smaller than in the two situations above. This situation shows that the influence of the regional-scale motion was greater than that for the previous two categories.

4. Regional-scale dominance (RD): In this category, wind direction at the study site was nearly uniform (extremely low R_{bj}) suggesting good ventilation (Allwine and Whiteman, 1994). The differences among R found at the 12 stations were even smaller than for the LWRS group, implying a strong increased influence of regional-scale motions. Indeed, the influence of regional-scale motions far outweighed the local ones for this category, and therefore, this group was considered to be dominated by strong regional-scale motions.

As shown in Table 1, the SOM classified 40% of cases were classified as LD, 29% were classified into RD, 17% and 14% were assigned into LSRW and LWRS respectively. These results indicate that most winter days in Baoji were strongly influenced by local-scale motions. Under LD, the average mass concentration of eBC_{fossil} (3.08 ± 2.07 μg m^{-3}) and $eBC_{biomass}$ (1.52 ± 1.19 μg m^{-3}) were the highest among all four atmospheric categories noted above and over half (60% for $eBC_{biomass}$ and 55% for eBC_{fossil}) of the high values (75^{th} to 100^{th} percentile) were found in this category (Figure 3). In addition, as shown in Figure 3, the vast majority of the high values are located in the zone indicating air stagnation ($S_{bj} \leq$ 130km, shaded yellow). One difference that the 75^{th} to 100^{th} percentile $eBC_{biomass}$ tended to cluster at $R_{bj} \leq 0.2$ indicates that under LD circumstances, pollutants were likely coming from the same directions as where the main pollution sources were agglomerated, but eBC_{fossil}, in contrast, evidently originated from more scattered locations ($R_{bj} \geq 0.4$). Under LSRW, the averaged mass concentrations of eBC_{fossil} and $eBC_{biomass}$ were 2.79 ± 1.73 μg $m^{-3}$and 1.06 ± 0.83 μg m^{-3} respectively (Table 1), which were both lower than those for the LD situation. When the regional scale of motion became stronger (i.e., LWRS and RD), the average mass concentration of eBC_{fossil} (2.15 ± 1.62 μg m^{-3} and 1.69 ± 1.36 μg m^{-3}) and $eBC_{biomass}$ (0.86 ± 1.58 μg m^{-3} and 0.93 ± 0.72 μg m^{-3}) were lower, presumably because strong winds cause the pollutants to mix with cleaner air. Interestingly, 19% of the total 75^{th} to 100^{th} percentile $eBC_{biomass}$ was found under RD, and 55% of that was when ventilation was good ($S_{bj} \geq$ 250km, $R_{bj} \leq 0.2$, Figure 3, shaded grey). These findings imply that the high mass concentrations of $eBC_{biomass}$ were carried by regional-scale airflow to the site.

Figure 4 portrays the mass concentrations of eBC_{fossil} and $eBC_{biomass}$ during the daytime and night time respectively under the four atmospheric motion categories specified earlier. As shown in Figure 4 (a) and (c), the mean values of both types of source-specific eBCs during daytime were the highest (3.02 ± 2.12 μg m^{-3} and 1.15 ± 0.8 μg m^{-3}) under LD and the lowest (1.36 ± 1.00 μg m^{-3} and 0.58 ± 0.53 μg m^{-3}) under RD. Meanwhile, the average mass concentrations of both types of eBC decreased when the influences of the regional scale of atmospheric motion getting were stronger. This suggests that eBC pollution was apt to accumulated under the dominance of local-scale motions and dispersed under the dominance of regional-scale motions during the daytime. Similar to the variations in the daytime, the mean values of eBC_{fossil} (3.00 ± 2.04 μg m^{-3}) and $eBC_{biomass}$ (1.76 ± 1.33 μg m^{-3}) under LD were also the highest during the night. However, unlike eBC_{fossil}, the mass concentrations of $eBC_{biomass}$ did not decrease when the influence of regional-scale atmospheric motions was stronger (Figure S12). The mean

value of $eBC_{biomass}$ under RD was the second highest (1.17 ± 0.73 μg m^{-3}). The nocturnal PBHL was higher than 100m (Figure S13) for the RD group, and therefore, the high nocturnal $eBC_{biomass}$ may have been caused by the $eBC_{biomass}$ transported to the site from upwind regions.

3.3 Impacts of air mass directions

Atmospheric motions can not only cause the dispersal of pollution but also bring polluted air to the site from distant sources. Indeed, air mass movements can mean the difference between no pollution and severe pollution at a receptor site. To examine the impacts caused by air masses from different directions, the hourly 24h-back trajectories were calculated at 100 m above the ground using the Hybrid Single-Particle Lagrangian Integrated Trajectory model (Draxler and Hess, 1998, Text S2). Then the trajectories were clustered by using an angle-based distance statistics method (Text S2) to show the general directional features. This method determines the direction from which the air masses reach the site and has been widely used for air mass trajectory clusters. A detailed method description can be found in Sirois and Bottenheim (1995). Three air-mass trajectory clusters were identified (Figure S14), 45% of total trajectories associated with Cluster No.1, which originated from the north. Cluster No.2 accounted for 36% of the trajectories, and those were from the east direction while Cluster No.3 composed 19% of the total trajectories and displayed origins from southwest.

Hourly trajectories were assigned into the four featured atmospheric motions. The varying concentrations of the source-specific eBCs associated with different clusters indicate the divergent impacts of air mass direction on the pollution level at the sampling site. As shown in Table 1, LD was mainly connected with the air masses from Cluster No.2 (52%) and Cluster No.1 (45%). The average mass concentrations of eBC_{fossil} and $eBC_{biomass}$ associated with Cluster No.1 were 2.82 ± 1.59 μg m^{-3} and 1.34 ± 1.07 μg m^{-3}. In comparison, Cluster No.2 was associated with a higher mean eBC_{fossil} (3.2 ± 1.73 μg m^{-3}) and the highest mean $eBC_{biomass}$ (1.72 ± 1.29 μg m^{-3}) of the three clusters. This could be attributed to more intensive emissions in the eastern parts of Baoji because 75% of the total population of Baoji is located in this area (http://tjj.baoji.gov.cn/art/2020/10/15/art_9233_1216737.html, accessed on 25 September 2021, in Chinese). Several highways and railways are located in the south and southwest of Baoji, but the population is sparse with only ~4% of the total population residing in those areas. Thus, Cluster No.3 was associated with the highest mean eBC_{fossil} concentration (3.64 ± 0.67 μg m^{-3}) but the lowest mean $eBC_{biomass}$ (0.67 ± 0.87 μg m^{-3}). It is important to point out, however, that only 3% of the total trajectories came from this cluster.

Under LSRW, 56% of the trajectories were from Cluster No.1, 33% from Cluster No.2, and 11% from Cluster No.3. Although the total averaged mass concentrations (Table 1) of two types of eBC generally showed that the regional-scale motions favored dissipation of eBC compared with LD, the eBC_{fossil} (3.43 ± 1.17 μg m^{-3}) associated with Cluster No.2 and $eBC_{biomass}$ associated with Cluster No.3. (1 ± 0.64 μg m^{-3}) were higher by 0.23 μg m^{-3} and 0.33μg m^{-3} respectively relative to the LD case. The rise of eBC_{fossil} associated with Cluster No.2 was possibly caused by the enhanced regional influence of pollutants brought from adjacent regions. According to previous studies (Wang et al., 2016; Xu et al., 2016), severe BC pollution in winter is caused by fossil fuel combustion in Xi'an which is to the east of Baoji. Studies also have reported that high EC emitted from biomass burning was found to have originated from Sichuan Province (Wu et al., 2020; Cai et al., 2018; Huang et al., 2020) which is to the southwest of Baoji. Combined with the phenomenon that the mass concentration of $eBC_{biomass}$ associated with Cluster No.3

rose with regional scales of motion, it is reasonable to conclude that the increase of $eBC_{biomass}$ associated with Cluster No.3 was likely influenced by pollution transport from the southwest.

Under LWRS, 42% of the trajectories were from Cluster No.1., 36% from Cluster No.3, and 22% from Cluster No.2. With stronger regional scales of motion, the mean values of eBC_{fossil} and $eBC_{biomass}$ associated with all clusters were lower than those under LD, except for $eBC_{biomass}$ associated with Cluster 3 which increased by 0.52 μg m^{-3}. As mentioned before, this increase could have been caused by regional transport.

In the last category (RD), 41% of the trajectories were from Cluster No.1., 39% from Cluster No.3, and 20% from Cluster No.2. Similar to the results for LWRS, the average mass concentration of eBC_{fossil} and $eBC_{biomass}$ associated with Cluster No.1 were only 35% and 48% of the respective values for LD. The average mass concentrations of eBC_{fossil} and $eBC_{biomass}$ associated with Cluster No.2 were 32% and 51% of the eBC_{fossil} and $eBC_{biomass}$ under LD. As for Cluster No.3, the average mass concentration of eBC_{fossil} associated with this cluster was also the lowest of all clusters. However, interestingly, the mean value of $eBC_{biomass}$ associated with Cluster No.3 was highest compared with other categories of Cluster No.3. Under strong influences of a regional scale of motions, the value of $eBC_{biomass}$ was 1.9 times as high as that under LD.

3.4 Radiative effects

Figure 5a shows the DREs at top of the atmosphere ($DRE_{eBC, TOA}$), surface ($DRE_{eBC, SUF}$), and the whole atmosphere ($DRE_{eBC, ATM}$) of eBC_{fossil} and $eBC_{biomass}$. The $DRE_{eBC, TOA}$ and $DRE_{eBC, SUF}$ of eBC were 13 W m^{-2} and -22.9 W m^{-2}, which were lower than that reported in Lanzhou (21.8 W m^{-2} and -47.5 W m^{-2} for $DRE_{eBC, TOA}$ and $DRE_{eBC, SUF}$) which is another river valley city in China (Zhao et al., 2019). This could be due to fact that the eBC mass concentration in Baoji was lower than in Lanzhou (Table S5). As for the $DRE_{eBC, TOA}$ and $DRE_{eBC, SUF}$ per an unit mass of BC, the results of the two studies were comparable. The $DRE_{eBC, TOA}$ of eBC_{fossil} ($DRE_{eBCfossil, TOA}$) and $eBC_{biomass}$ ($DRE_{eBCbiomass, TOA}$) were 9.4 ± 7.5 W m^{-2} and 3.6 ± 3.4 W m^{-2} indicating a warming effect at the top of the atmosphere. The $DRE_{eBC, SUF}$ of eBC_{fossil} ($DRE_{eBCfossil, SUF}$) and $eBC_{biomass}$($DRE_{eBCbiomass, SUF}$) were -16.5 ± 13.5 W m^{-2} and -6.4 ± 6.2 W m^{-2} showing a cooling effect at the surface. The $DRE_{eBC, ATM}$ of eBC_{fossil} ($DRE_{eBCfossil, ATM}$) and $eBC_{biomass}$ ($DRE_{eBCbiomass, ATM}$) were 25.9 ± 20.8 W m^{-2} and 10 ± 9.5 W m^{-2} in the atmosphere, indicating a heating effect.

Figure 5 also shows the $DRE_{eBC, ATM}$ of the source-specific eBC for different atmospheric motions. In general, the changes of $DRE_{eBC, ATM}$ are in accordance with those of the eBC mass concentrations. The $DRE_{eBCfossil, ATM}$ under LD was the largest with a mean value of 30.4 ± 23 W m^{-2}, followed by LSRW (28.7 ± 20.7 W m^{-2}). As the mass concentration of eBC_{fossil} was low when regional scales of motion were stronger, the $DRE_{eBC, ATM}$ under LWRS and RD were also lower compared with those under LD or LSRW. By contrast, the $DRE_{eBC, ATM}$ of $eBC_{biomass}$ under LSRW was the highest (11.5 ± 11.8 W m^{-2}), but it is only 0.3 W m^{-2} higher than that under LD. When the regional scale of motions became stronger, the $DRE_{eBCbiomass, ATM}$ declined as expected due to the lower $eBC_{biomass}$ mass concentrations (Figure 4c). The $DRE_{eBC, ATM}$ of $eBC_{biomass}$ under LWRS and RD were 8.6 ± 8.5 W m^{-2} and 7.9 ± 7.4 W m^{-2} respectively.

Although $DRE_{eBC, ATM}$ declined with increased influences from the regional scale of motion, the $DRE_{eBC, ATM}$ efficiency ($DRE_{eBC, ATM}$ per mass concentration) was found to increase with greater regional-scale motion. Furthermore, the DRE efficiencies of both types of eBC under LD and LSRW were comparable, around 10 W m^{-2} (Table 2). In contrast, the efficiencies

varied more when the regional-scale motions were stronger. Under LWRS, the efficiencies of eBC_{fossil} and $eBC_{biomass}$ were 13.5 ± 6.7 and 14.7 ± 8.1 (W m^{-2})/(μg m^{-3}) respectively. Under RD, the efficiencies were even higher, 15.6 ± 8.9 (W m^{-2})/(μg m^{-3}) for eBC_{fossil} and 15.5 ± 8.4 (W m^{-2})/(μg m^{-3}) for $eBC_{biomass}$, which are > 1.5 times those recorded under LD. The higher eBC efficiencies may have been caused by the increases in the BC MAC during the regional transport. Studies have confirmed that the aging processes in the atmosphere can enhance the light-absorbing ability of BC (Chen et al., 2017; Shen et al., 2014), and regional transport can provide sufficient time for BC aging (Shiraiwa, et al. 2007; Cho et al., 2021). Therefore, the nonlinear change between mass concentration and DRE efficiency was very likely caused by the strong regional-scale motions that dispersed fresh BC from local emissions but also brought aged BC to the area from the upwind regions. As a result, under these conditions, the transported BC reached a receptor site with a higher light-absorbing ability which led to a higher DRE efficiency of BC at the sampling site. This strongly implies regionally transported BC can greatly perturb climate, particularly at the river-valley city in our study where dispersion was weak (Zhao et al., 2015; Wang et al., 2013).

4 Conclusions

This study derived site-specific AAEs using a PMF model for which chemical and optical data collected from a river-valley city during winter were used as the inputs. Based on the calculated AAEs, source-specific eBCs (i.e., eBC_{fossil} and $eBC_{biomass}$) were then apportioned using an aethalometer model. Finally, the impacts of different scales of atmospheric motions on the mass concentrations of the source-specific eBCs and the induced DREs were investigated. Four sources of eBC were identified: which are diesel vehicular emissions, biomass burning, coal combustion, and mineral dust. The derived AAEs were 1.07 for diesel vehicular emissions, 2.13 for biomass burning, 1.74 for coal combustion, and 1.78 for mineral dust. The mean values of eBC_{fossil} and $eBC_{biomass}$ were 2.46 μg $m^{-3}$and 1.17 μg m^{-3}, respectively.

The self-organizing map indicated that there were four types of atmospheric motions during the sampling period that affected the mass concentrations of source-specific eBCs. Of these, the local-scale motions were the main influence on most winter days. The eBC_{fossil} and $eBC_{biomass}$ under those identified atmospheric motions showed that over half of the 75^{th} to 100^{th} percentile values for the entire data set were found in LD group (60% for $eBC_{biomass}$ and 55% for eBC_{fossil}). This illustrates that the BC pollution was more severe under the influences of local-scale motion outweighed regional-scale motions. However, even though regional-scale motions were associated with lower eBCs, 19% of the high values of $eBC_{biomass}$ values occurred under RD, especially when there was good ventilation. Furthermore, the air masses from different directions also had impacts on the source-specific eBCs that varied relative to the different atmospheric motions. eBC_{fossil} most likely accumulated under the influence of strong local-scale motions, but $eBC_{biomass}$ also was found to be increased with the enhanced regional scale of motions when the air masses from the southwest; this indicates that there were impacts from regional transport.

Similar to the mass concentrations, the DREs of the two types of eBC were both lower when the regional scale of motions were greater than the local ones. However, the changes in mass concentrations and DREs were not proportionate because the regional-scale of motions carried the fresh BC away from the local site but brought the aged BCs to the site from the upwind regions. As a result, the DRE efficiency of eBC was ~1.5 times higher when the regional scale of motion was stronger. This study showed that different scales of air motions affected the mass concentrations of source-specific eBCs and their DRE efficiencies. More specifically our study highlights importance of regional transport for the BC radiative forcing and shows

how the enhancement of BC radiative effects caused by aging during regional transport could have especially significant implications for sites in river valleys. The relationships between BC and atmospheric scales of motion should be evaluated for other environments besides river valley cities because quantitative information on the relative importance of locally emitted versus regionally transported materials will be useful for developing pollution controls and for predicting future changes in climate.

Data availability. The data are available from the authors upon request.

Supplement. The supplement related to this article is available online.

Author contributions. QW and JC designed the study. BZ and SL conducted the field measurements. YQ and JT conducted data analysis. SL and TZ performed the chemical analysis of filters. HL draft the article and QW revised it. JC and YH commented on the paper.

Competing interests. The authors declare that they have no conflict of interest.

Acknowledgments. This research has been supported by the National Natural Science Foundation of China (42192512), the Key Research and Development Program of Shaanxi Province (2018-ZDXM3-01), the Key Project of CAS (ZDRW-ZS-2017-6), and the Youth Innovation Promotion Association of the Chinese Academy of Sciences (2019402).

Reference

Amato, F., Alastuey, A., Karanasiou, A., Lucarelli, F., Nava, S., Calzolai, G., Severi, M., Becagli, S., Gianelle, V. L., Colombi, C., Alves, C., Custódio, D., Nunes, T., Cerqueira, M., Pio, C., Eleftheriadis, K., Diapouli, E., Reche, C., Minguillón, M. C., Manousakas, M.-I., Maggos, T., Vratolis, S., Harrison, R. M., and Querol, X.: AIRUSE-LIFE+: a harmonized PM speciation and source apportionment in five southern European cities, Atmos. Chem. Phys., 16, 3289–3309, https://doi.org/10.5194/acp-16-3289-2016, 2016.

Artaxo, P., Fernandas, E. T., Martins, J. V., Yamasoe, M. A., Maenhaut, W., Longo, K. M., Castanho, A., and Hobbs, P. V.: Large-scale aerosol source apportionment in Amazonia, J. Geophys. Res.-Atmos., 103, 31837–31847, https://doi.org/10.1029/98jd02346, 1998.

Allwine, K. J., and Whiteman, C. D.: Single-station integral measures of atmospheric stagnation, recirculation and ventilation. Atmos. Environ., 28: 713–721, https://doi.org/10.1016/1352-2310(94)90048-5, 1994.

Bei, N., Li, G., Huang, R., Cao, J., Meng, N., Feng, T., Liu, S., Zhang, T., Zhang, Q., and Molina, L.: Typical synoptic situations and their impacts on the wintertime air pollution in the Guanzhong basin, China, Atmos. Chem. Phys., 16, 7373–7387, http://dx.doi.org/10.5194/acp-16-7373-2016, 2016.

Bond, T. C., Doherty, S. J., Fahey, D. W., Forster, P. M., Berntsen, T., DeAngelo, B. J., Flanner, M. G., Ghan, S., Karcher, B., Koch, D., Kinne, S., Kondo, Y., Quinn, P. K., Sarofim, M. C., Schultz, M. G., Schulz, M., Venkataraman, C., Zhang, H., Zhang, S., Bellouin, N., Guttikunda, S. K., Hopke, P. K., Jacobson, M. Z., Kaiser, J. W., Klimont, Z., Lohmann, U., Schwarz, J. P., Shindell, D., Storelvmo, T., Warren, S. G., and Zender, C. S.: Bounding the role of black carbon in the climate system: A scientific assessment, J. Geophys. Res.-Atmos., 118, 5380–5552, https://doi.org/10.1002/jgrd.50171, 2013.

Brown, S. G., Eberly, S., Paatero, P., and Norris, G. A.: Methods for estimating uncertainty in PMF solutions: Examples with ambient air and water quality data and guidance on reporting PMF results, Sci. Total Environ., 518–519, 626–635, https://doi.org/10.1016/j.scitotenv.2015.01.022, 2015.

Brulfert, G., Chemel, C., Chaxel, E., Chollet, J., Jouve, B., and Villard, H.: Assessment of 2010 air quality in two Alpine valleys from modelling: weather type and emission scenarios, Atmos. Environ., 40, 7893–7907, https://doi.org/10.1016/j.atmosenv.2006.07.021, 2006.

549 Cao, J. J., Zhu, C. S., Tie, X. X., Geng, F. H., Xu, H. M., Ho, S. S. H., Wang, G. H., Han, Y. M., and Ho, K. F.: Characteristics
550 and sources of carbonaceous aerosols from Shanghai, China, Atmos. Chem. Phys., 13, 803-817,
551 https://doi.org/10.5194/acp-13-803-2013, 2013.

552 Cai, S., Ma, Q., Wang, S., Zhao, B., Brauer, M., Cohen, A., Martin, R., Zhang, Q., Li, Q., Wang, Y., Hao, J., Frostad, J.,
553 Forouzanfar, M., and Burnett, R.: Impact of air pollution control policies on future $PM_{2.5}$ concentrations and their source
554 contributions in China, J. Environ. Manage., 227, 124–133, https://doi.org/10.1016/j.jenvman.2018.08.052, 2018.

555 Cappa, C. D., Onasch, T. B., Massoli, P., Worsnop, D. R., Bates, T. S., Cross, E. S., Davidovits, P., Hakala, J., Hayden, K. L.,
556 Jobson, B. T., Kolesar, K. R., Lack, D. A., Lerner, B. M., Li, S.-M., Mellon, D., Nuaaman, I., Olfert, J. S., Petäjä, T.,
557 Quinn, P. K., Song, C., Subramanian, R., Williams, E. J., and Zaveri, R. A.: Radiative absorption enhancements due to
558 the mixing state of atmospheric black carbon, Science., 337, 1078–1081, https://doi.org/10.1126/science.1223447, 2012.

559 Carvalho, A.C., Carvalho, A., Gelpi, I., Barreiro, M., Borrego, C., Miranda, A., and Perez-Munuzuri, V.: Influence of
560 topography and land use on pollutants dispersion in the Atlantic coast of Iberian Peninsula, Atmos. Environ., 40,3969–
561 3982, https://doi.org/10.1016/j.atmosenv.2006.02.014, 2006.

562 Cho, C., Schwarz, J., Perriing, A., Lamb, K., Kondo, Y., Park, J., Park, D., Shim, K., Park, J., Park, R., Lee, M., Song, C., Kim,
563 S.: Light-absorption enhancement of black carbon in the Asian outflow inferred from airborne SP2 and in-situ
564 measurements during KORUS- AQ, Sci. Total Environ., 773, 145531, https://doi.org/10.1016/j.scitotenv.2021.145531,
565 2021.

566 Chang, F., Chang, L., Kang, C., Wang, Y., Huang, A.: Explore spatio-temporal $PM_{2.5}$ features in northern Taiwan using
567 machine learning techniques, Sci. Total Environ., 736, 139656, https://doi.org/10.1016/j.scitotenv.2020.139656, 2020.

568 Cheng, Y., He, K., Zheng, M., Duan, F., Ma, Y., Tan, J., Yang, F., Liu, J., Zhang, X., Weber, R., Bergin, M. and Russell, A.:
569 Mass absorption efficiency of elemental carbon and water-soluble organic carbon in Beijing, China, Atmos. Chem. Phys.,
570 11, 11497–11510, https://doi:10.5194/acp-11-11497-2011, 2011.

571 Chen, X., Wang, Z., Yu, F., Pan, X., Li, J., Ge, B., Wang, Z., Hu, M., Yang, W., Chen, H.: Estimation of atmospheric aging
572 time of black carbon particles in the polluted atmosphere over central-eastern China using microphysical process analysis
573 in regional chemical transport model, Atmos. Environ., 163,44-56, https://doi.org/10.1016/j.atmosenv.2017.05.016, 2017

574 Drinovec, L., Močnik, G., Zotter, P., Prévôt, A. S. H., Ruckstuhl, C., Coz, E., Rupakheti, M., Sciare, J., Müller, T.,
575 Wiedensohler, A., and Hansen, A. D. A.: The "dual-spot" Aethalometer: an improved measurement of aerosol black
576 carbon with real-time loading compensation, Atmos. Meas. Tech., 8, 1965-1979, https://doi.org/10.5194/amt-8-1965-2015,
577 2015.

578 Draxler, R., and Hess, G.: An overview of the HYSPLIT_4 modelling system for trajectories, Aust. Meteorol. Mag., 47, 1998.

579 Dutton, J., The ceaseless wind an introduction to the theory of atmospheric motion, McGraw-Hill, Inc., U.S.A., 1976

580 Geivanidis, S., Pistikopoulos, P., and Samaras, Z.: Effect on exhaust emissions by the use of methylcyclopentadienyl
581 manganese tricarbonyl (MMT) fuel additive and other lead replacement gasolines. Sci. Total Environ., *305*, 129-141,
582 https://doi.org/10.1016/S0048-9697(02)00476-X, 2003.

583 Glojek, K., Moˇcnik, G., Alas, H., Cuesta-Mosquera, A., Drinovec, L., Gregoriˇc, A., Ogrin, M., Ježek, I., Müller, T., Rigler,
584 M., Remškar, M., Pinxteren, D., Herrmann, H., Ristorini, M., Merkel, M., Markelj, M., Wiedensohler, A.: The impact of
585 temperature inversions on black carbon and particle mass concentrations in a mountainous area, Atmos. Chem. Phys., 22,
586 5577–5601, https://doi.org/10.5194/acp-22-5577-2022, 2022.

587 Green, M., Chow, J., and Watson, G.: Effects of snow cover and atmospheric stability on winter $PM_{2.5}$ concentrations in western
588 U.S. valleys, J. Appl. Meteorol. Clim., 54, https://doi.org/doi: 10.1175/JAMC-D-14-0191.1, 2016.

589 Han, H., Liu, J., Shu, L., Wang, T., and Yuan, H.: Local and synoptic meteorological influences on daily variability in
590 summertime surface ozone in eastern China, Atmos. Chem. Phys., 20, 203–222, https://doi.org/10.5194/acp-20-203-2020,
591 2020.

592 Helin, A., Niemi, J. V., Virkkula, A., Pirjola, L., Teinilä, K., Backman, J., Aurela, M., Saarikoski, S., Rönkkö, T., Asmi, E.,
593 and Timonen, H.: Characteristics and source apportionment of black carbon in the Helsinki metropolitan area, Finland,
594 Atmos. Environ., 190, 87-98, https://doi.org/10.1016/j.atmosenv.2018.07.022, 2018.

He, C., Liou, K.-N., Takano, Y., Zhang, R., Levy Zamora, M., Yang, P., Li, Q., and Leung, L. R.: Variation of the radiative properties during black carbon aging: theoretical and experimental intercomparison, Atmos. Chem. Phys., 15, 11967–11980, https://doi.org/10.5194/acp-15-11967-2015, 2015.

Hewitson, B. C. and Crane, R. G.: Consensus between GCM climate change projections with empirical downscaling: precipitation downscaling over South Africa, Int. J. Climatol., 26, 1315–1337, https://doi.org/10.1002/joc.1314, 2006.

Hsu, C.-Y., Chiang, H.-C., Lin, S.-L., Chen, M.-J., Lin, T.-Y., and Chen, Y.-C.: Elemental characterization and source apportionment of PM_{10} and $PM_{2.5}$ in the western coastal area of central Taiwan, Sci. Total Environ., 541, 1139-1150, https://doi.org/10.1016/j.scitotenv.2015.09.122, 2016.

Huang, Y., Zhang, L., Li, T., Chen, Y., and Yang, F.: Seasonal variation of carbonaceous species of $PM_{2.5}$ in a small city in Sichuan Basin, China, Atmosphere., 11, 1286, https://doi.org/10.3390/atmos11121286, 2020.

Jacobson, M. Z.: Control of fossil-fuel particulate black carbon and organic matter, possibly the most effective method of slowing global warming, J. Geophys. Res., 107, 4410, https://doi.org/10.1029/2001JD001376, 2002.

Jiang, N. B., Scorgie, Y., Hart, M., Riley, M. L., Crawford, J., Beggs, P. J., Edwards, G. C., Chang, L. S., Salter, D., and Virgilio, G. D.: Visualising the relationships between synoptic circulation type and air quality in Sydney, a subtropical coastal-basin environment, Int. J. Climatol., 37, 1211–1228, https://doi.org/10.1002/joc.4770, 2017.

Kant, Y., Shaik,D., S., Mitra, D., Chandola, H., Babu, S. S., and Chauhan, P., Black carbon aerosol quantification over north-west himalayas: seasonal heterogeneity, source apportionment and radiative forcing, Environ. Pollut., 10.1016/j.envpol.2019.113446, 2019.

Kangas, J., and Kohonen, T.: Developments and applications of the self-organizing map and related algorithms, Math. Comput. Simulat., 41, 3-12, https://doi.org/10.1016/0378-4754(96)88223-1, 1996.

Kahnert, M., and Kanngiesser, F.: Review: modelling optical properties of atmospheric black carbon aerosols. J. Quant. Spectrosc., RA, 244, 106849, https://doi.org/10.1016/j.jqsrt.2020.106849, 2020.

Kalthoff, N., Horlacher, V., Corsmeier, U., Volz-Thomas, A., Kolahgar, B., Geiß, H., Möllmann-Coers, M., and Knaps, A.: Influence of valley winds on transport and dispersion of airborne pollutants in the Freiburg-Schauinsland area, J. Geophys. Res.-Atmos., 105, 1585–1597, https://doi.org/10.1029/1999jd900999, 2000.

Kirchstetter, T. W., Novakov, T., and Hobbs, P. V.: Evidence that the spectral dependence of light absorption by aerosols is affected by organic carbon, J. Geophys. Res.-Atmos., 109, D21208, https://doi.org/10.1029/2004jd004999, 2004.

Kohonen, T.: The self-organizing map, Proc. IEEE, 78, 1464–1480, https://doi.org/10.1109/5.58325, 1990.

Kohonen, T., and Simula, O., Visa, A., Kangas, J.: Engineering applications of the aelf-organizing map, P. IEEE, 84(10), 1358-1384, https://doi.org/10.1109/5.537105,1996.

Liao, Z., Xie, J., Fang, X., Wang, Y., Zhang, Y., Xu, X., and Fan, S.: Modulation of synoptic circulation to dry season $PM_{2.5}$ pollution over the Pearl River Delta region: An investigation based on self-organizing maps. Atmos. Environ., 230, 117482, https://doi.org/10.1016/j.atmosenv.2020.117482, 2020.

Liu, S., Gautam, A., Yang, X., Tao, J., Wang, X., Zhao, W: Analysis of improvement effect of $PM_{2.5}$ and gaseous pollutants in Beijing based on self-organizing map network, Sustain. Cities Soc., 70, 102827, https://doi.org/10.1016/j.scs.2021.102827, 2021.

Lewis, C. W., Norris, G. A., Conner, T. L., and Henry, R. C.: Source apportionment of Phoenix $PM_{2.5}$ aerosol with the unmix receptor model, J. Air Waste Manage., 53, 325–338, https://doi.org/10.1080/10473289.2003.10466155, 2003.

Levy, I., Dayan, U., and Mahrer, Y.: Differing atmospheric scales of motion and their impact on air pollutants, Int. J. Climatol., 30, 612–619, https://doi.org/10.1002/joc.1905, 2010.

Lin, Y., Tsai, C., Wu, T., Zhang, R., Chi, K., Huang, Y., Lin, S., and Hsu, S.: Characteristics of trace metals in traffic-derived particles in Hsuehshan Tunnel, Taiwan: size distribution, potential source, and fingerprinting metal ratio, Atmos. Chem. Phys., 15, 4117–4130, https://doi.org/10.5194/acp-15-4117-2015, 2015.

IPCC: Climate Change 2021: The physical science basis. contribution of working group i to the sixth assessment report of the intergovernmental panel on climate change [Masson-Delmotte, V., P. Zhai, A. Pirani, S.L. Connors, C. Péan, S. Berger,

N. Caud, Y. Chen, L. Goldfarb, M.I. Gomis, M. (eds)], https://reliefweb.int/report/world/climate-change-2021-physical-science-basis, 2021

Manousakas, M., Papaefthymiou, H., Diapouli E., Migliori, A., Karydas, A.G., Bogdanovic-Radovic, I., Eleftheriadis, K.: Assessment of $PM_{2.5}$ sources and their corresponding level of uncertainty in a coastal urban area using EPA PMF 5.0 enhanced diagnostics, Sci. Total Environ., 574, 155–164, https://doi.org/10.1016/j.scitotenv.2016.09.047, 2017.

Manö, S., and Andreae, M.O.: Emission of methyl bromide from biomass burning. Science., 263, 1255–1257, https://doi.org/10.1126/science.263.5151.1255, 1994.

Norris, G., Duvall, R., Brown, S. and Bai, S.: EPA Positive Matrix Factorization (PMF) 5.0 fundamentals and user guide prepared for the US Environmental Protection Agency Office of 30 research and development, Washington, DC, by the National Exposure Research Laboratory, Research Triangle Park; Sonoma Technology, Inc., Petaluma., https://www.epa.gov/air-research/epa-positive-matrix-factorization-50-fundamentals-and-user-guide, 2014.

Ochoa-Hueso, R., Munzi, S., Alonso, R., Arróniz-Crespo, M., Avila, A., Bermejo, V., Bobbink, R., Branquinho, C., Concostrina-Zubiri, L., Cruz, C., Cruz de Carvalho, R., De Marco, A., Dias, T., Elustondo, D., Elvira, S., Estébanez, B., Fusaro, L., Gerosa, G., Izquieta-Rojano ,S., Lo Cascio, M., Marzuoli, R., Matos, P., Mereu, S., Merino, J., Morillas, L., Nunes, A., Paoletti, E., Paoli, L., Pinho, P., Rogers, I.B., Santos, A., Sicard, P., Stevens, C. J., and Theobald, M. R.: Ecological impacts of atmospheric pollution and interactions with climate change in terrestrial ecosystems of the Mediterranean Basin: current research and future directions, Environ. Pollut., 227, 194–206, 2017.

Oke, T., Boundary layer climates, 2nd edition, Taylor & Francis e-Library, 2002.

Panicker, A. S., Pandithurai, G., Safai, P. D., Dipu, S., and Lee, D.-I.: On the contribution of black carbon to the composite aerosol radiative forcing over an urban environment, Atmos. Environ., 44, 3066-3070, 10.1016/j.atmosenv.2010.04.047, 2010.

Pathak, B., Kalita, G., Bhuyan, K., Bhuyan, P. and Moorthy, K.: Aerosol temporal characteristics and its impact on shortwave radiative forcing at a location in the northeast of India, J. Geophys. Res.-Atmos., 115, D19204, https://doi:10.1029/2009JD013462, 2010.

Peng, J., Hu, M., Guo, S., Du, Z., Zheng, J., Shang, D., Levy, M., and Zeng, L.: Markedly enhanced absorption and direct radiative forcing of black carbon under polluted urban environments, P. Natl. Acad. Sci. USA, 113, 4266–4271, https://doi.org/10.1073/pnas.1602310113, 2016.

Pearce, J. L., Waller, L. A., Chang, H. H., Klein, M., Mulholland, J. A., Sarnat, J. A., Sarnat, S. E., Strickland, M. J., and Tolbert, P. E.: Using self-organizing maps to develop ambient air quality classifications: a time series example, Environ. Health-Glob., 13, https://doi.org/10.1186/1476-069X-13-56, 2014.

Ramachandran A., Rustum, R., and Adeloye, A.: Anaerobic digestion process modeling using Kohonen self-organising maps, Heliyon, 5,e01511, https://doi.org/10.1016/j.heliyon.2019.e01511, 2019.

Rajesh, T. A., and Ramachandran, S.: Black carbon aerosols over urban and high altitude remote regions: characteristics and radiative implications, Atmos. Environ., 194, 110-122, https://doi.org/10.1016/j.atmosenv.2018.09.023, 2018.

Reusch, D.B., Alley, R.B., and Hewitson, B.C.: Relative performance of self-organizing maps and principal component analysis in pattern extraction from synthetic climatological data. Polar Geogr., 29(3): 188–212. http://dx.doi.org/10.1080/789610199, 2005.

Ricchiazzi, P., Yang, S., Gautier, C., and Sowle, D.: SBDART: A research and teaching software tool for plane-parallel radiative transfer in the Earth's atmosphere, B. Am. Meteorol. Soc., 79, 2101–2114, https://doi.org/10.1175/1520-0477(1998)0792.0.CO;2, 1998.

Sandradewi, J., Prévôt, A. S. H., Weingartner, E., Schmidhauser, R., Gysel, M., and Baltensperger, U.: A study of wood burning and traffic aerosols in an Alpine valley using a multi-wavelength Aethalometer, Atmos. Environ., 42, 101-112, https://doi.org/10.1016/j.atmosenv.2007.09.034, 2008.

Seinfeld, J., and Pandis, S., 2006. Atmospheric chemistry and physics: from air pollution to climate change, 2nd ed., Published by John Wiley & Sons, Inc., Hoboken, New Jersey, United States of America,

Schroter, D., Cramer, W., Leemans, R., Prentice, C., Araujo, M., Arnell, N., Bondeau, A., Bugmann, H., Carter, T., Gracia, C., de la Vega-Leinert, A., Erhard, M., Ewert, F., Glendining, M., House, J., Kankaanpaa, S., Klein, R., Lavorel, S., Lindner, M., Metzger, M., Meyer, J., Mitchell, T., Reginster, I., Rounsevell, M., Sabate, S., Sitch, S., Smith, B., Smith, J., Smith, P., Sykes, ´ M., Thonicke, K., Thuiller, W., Tuck, G., Zaehle, S., and Zierl, B.: Ecosystem service supply and vulnerability to global change in Europe, Science., 310, 1333–1337, https://doi.org/10.1126/science.1115233, 2005.

Shen, Z., Liu, J., Horowitz, W., Henze, D., Levy, H., Mauzerall, D., Lin, J., and Tao, S.: Analysis of transpacific transport of black carbon during HIPPO-3: implications for black carbon aging, Atmos. Chem. Phys., 14, 6315–6327, https://doi.org/10.5194/acp-14-6315-2014, 2014.

Shiraiwa, M., Kondo, Y., Moteki, N., Takegawa, N., Miyazaki, Y., and Blake, D. R.: Evolution of mixing state of black carbon in polluted air from Tokyo, Geophys. Res. Letters., 34, L16803, https://doi.org/10.1029/2007GL029819, 2007.

Shindell, D., Kuylenstierna, J. C. I., Vignati, E., van Dingenen, R., Amann, M., Klimont, Z., Anenberg, S. C., Muller, N., JanssensMaenhout, G., Raes, F., Schwartz, J., Faluvegi, G., Pozzoli, L., Kupiainen, K., Hoglund-Isaksson, L., Emberson, L., Streets, D., Ramanathan, V., Hicks, K., Oanh, N. T. K., Milly, G., Williams, M., Demkine, V., and Fowler, D.: Simultaneously mitigating near-term climate change and improving human health and food security, Science, 335, 183–189, https://doi.org/10.1126/science.1210026, 2012.

Sirois, A. and Bottenheim, J. W.: Use of backward trajectories to interpret the 5-year record of PAN and O_3 ambient air concentrations at Kejimkujik National Park, Nova Scotia, J. Geophys. Res., 100, 2867–2881, https://doi.org/10.1029/94JD02951, 1995.

Song, Y., Zhang, Y., Xie, S., Zeng, L., Zheng, M., Salmon, L. G., Shao, M., and Slanina, S.: Source apportionment of $PM_{2.5}$ in Beijing by positive matrix factorization, Atmos. Environ., 40, 1526-1537, https://doi.org/10.1016/j.atmosenv.2005.10.039, 2006.

Sun, J., Zhi, G., Hitzenberger, R., Chen, Y., Tian, C., Zhang, Y., Feng, Y., Cheng, M., Zhang, Y., Cai, J., Chen, F., Qiu, Y., Jiang, Z., Li, J., Zhang, G., and Mo, Y.: Emission factors and light absorption properties of brown carbon from household coal combustion in China, Atmos. Chem. Phys., 17, 4769–4780, https://doi.org/10.5194/acp-17-4769-2017, 2017.

Stauffer, R. M., Thompson, A. M., and Young, G. S.: Tropospheric ozonesonde profiles at long-term US monitoring sites: 1. A climatology based on self-organizing maps, J. Geophys. Res.-Atmos, 121, 1320–1339, https://doi.org/10.1002/2015JD023641, 2016.

Tan, J., Zhang, L. Zhou, X., Duan, J. Li, Y., Hu, J., and He, K.: Chemical characteristics and source apportionment of $PM_{2.5}$ in Lanzhou, China, Sci. Total Environ., 601, 1743-1752, https://doi.org/10.1016/j.scitotenv.2017.06.050, 2017.

Tao, J., Zhang L., Zhang, R., Wu, Y., Zhang, Z., Zhang, X., Tang. Y., Cao, J., and Zhang, Y.: Uncertainty assessment of source attribution of PM2.5 and its water-soluble organic carbon content using different biomass burning tracers in positive matrix factorization analysis — a case study in Beijing, China, Sci. Total Environ., 543, 326–335, https://doi.org/10.1016/j.scitotenv.2015.11.057, 2016.

Tao, J., Zhang, L. M., Cao, J. J., Zhong, L. J., Chen, D. S., Yang, Y. H., Chen, D. H., Chen, L. G., Zhang, Z. S., Wu, Y. F., Xia, Y. J., Ye, S. Q., and Zhang, R. J.: Source apportionment of $PM_{2.5}$ at urban and suburban areas of the Pearl River Delta region, south China – with emphasis on ship emissions, Sci. Total Environ., 574, 1559–1570, https://doi.org/10.1016/j.scitotenv.2016.08.175, 2017.

Thorpe, A., and Harrison, R. M.: Sources and properties of non-exhaust particulate matter from road traffic: a review, Sci. Total Environ., *400*, 270-282, https://doi.org/10.1016/j.scitotenv.2008.06.007, 2008.

Urban, R. C., Lima-Souza, M., Caetano-Silva, L., Queiroz, M. E. C., Nogueira, R. F. P., Allen, A. G., Cardoso, A. A., Held, G., and Campos, M. L. A. M.: Use of levoglucosan, potassium, and water-soluble organic carbon to characterize the origins of biomass-burning aerosols, Atmos. Environ., 61, 562-569, https://doi.org/10.1016/j.atmosenv.2012.07.082, 2012.

Washenfelder, R., Attwood, A., Brock, C., Guo, H., Xu, L., Weber, R., Ng, N., Allen, H., Ayres, B., Baumann, K., Cohen, R., Draper, D., Duffey, K., Edgerton, E., Fry, J., Hu, W., Jimenez, J., Palm, B., Romer, P., Stone, E., Wooldridge, P., and Brown, S.: Biomass burning dominates brown carbon absorption in the rural southeastern United States, Geophys. Res. Lett., 42, 653–664, https://doi.org/10.1002/2014GL062444, 2015

Wang, Q., Huang, R., Zhao, Z., Cao, J., Ni, H., Tie, X., Zhao, S., Su, X., Han, Y., Shen, Z., Wang, Y., Zhang, N., Zhou, Y., and Corbin, J.: Physicochemical characteristics of black carbon aerosol and its radiative impact in a polluted urban area of China, J. Geophys. Res. Atmos., 121, https://doi.org/doi:10.1002/2016JD024748, 2016.

Wang, Q., Han, Y., Ye, J., Liu, S., Pongpiachan, S., Zhang, N., Han, Y., Tian, J., Wu, C., Long, X., Zhang, Q., Zhang, W., Zhao, Z., and Cao, J.: High contribution of secondary brown carbon to aerosol light absorption in the southeastern margin of Tibetan Plateau, Geophys. Res. Lett., 46, 4962–4970, https://doi.org/10.1029/2019GL082731, 2019.

Wang, Q., Liu, H., Wang, P., Dai, W., Zhang T., Zhao, Y., Tian, J., Zhang, W., Han, Y., and Cao, J.: Optical source apportionment and radiative effect of light-absorbing carbonaceous aerosols in a tropical marine monsoon climate zone: the importance of ship emissions, Atmos. Chem. Phys., 20, 15537–15549, https://doi.org/10.5194/acp-20-15537-2020, 2020.

Wang, W., Chen, N., and Ma, X., Characteristic analysis on mountain-valley wind in deep valley, Adv. Mater., Vols 610-613, pp 817-824, https://doi:10.4028/www.scientific.net/AMR.610-613.817, 2013.

Wei, N., Wang, N., Huang, X., Liu, P., and Chen, L.: The effects of terrain and atmospheric dynamics on cold season heavy haze in the Guanzhong Basin of China, Atmos. Pollut. Res., 11, 1805-1819, https://doi.org/10.1016/j.apr.2020.07.007, 2020.

Wehrens, R., and Kruisselbrink, J.: Supervised and unsupervised self-organising maps, Package 'kohonen', 2019, https://cran.r-project.org/.

Wu, J., Kong, S., Wu, F., Cheng, Y., Zheng, S., Qin, S., Liu, X., Yan, Q., Zheng, H., Zheng, M., Yan, Y., Liu, D., Ding, S., Zhao, D., Shen, G., Zhao, T., and Qi, S.: The moving of high emission for biomass burning in China: view from multiyear emission estimation and human-driven forces, Environ. Int., 142, 105812, https://doi.org/10.1016/j.envint.2020.105812, 2020.

Wu, C. and Yu, J. Z.: Determination of primary combustion source organic carbon-to-elemental carbon (OC / EC) ratio using ambient OC and EC measurements: secondary OC-EC correlation minimization method, Atmos. Chem. Phys., 16, 5453–5465, https://doi.org/10.5194/acp-16-5453-2016, 2016.

Xiao, S., Wang, Q., Cao, J., Huang, R., Chen, W., Han, Y., Xu, H., Xu, H., Liu, S., Zhou, Y., Wang, P., Zhang, J., Zhan, C.: Long-term trends in visibility and impacts of aerosol composition on visibility impairment in Baoji, China, Atmos. Res., 149, 88–95, http://dx.doi.org/10.1016/j.atmosres.2014.06.006, 2014.

Xu, H. M., Cao, J. J., Ho, K. F., Ding, H., Han, Y. M., Wang, G. H., Chow, J. C., Watson, J. G., Khol, S. D., Qiang, J., and Li, W. T.: Lead concentrations in fine particulate matter after the phasing out of leaded gasoline in Xi'an, China, Atmos. Environ., 46, 217– 224, https://doi.org/10.1016/j.atmosenv.2011.09.078, 2012.

Xu, H., Ren, Y., Zhang, W., Meng,W., Yun, X., Yu, X., Li, J., Zhang, Y., Shen, G., Ma, J., Li, B., Cheng, H., Wang, X., Wan, Y., and Tao, S.: Updated global black carbon emissions from 1960 to 2017: improvements, trends, and drivers, Environ. Sci. Technol., 55, 7869-7879, https://doi.org/10.1021/acs.est.1c03117, 2021.

Xu, H., Cao, J., Chow, J., Huang, R., Shen, Z., Chen, L.W., Ho, K., Watson, J.: Inter-annual variability of wintertime $PM_{2.5}$ chemical composition in Xi'an, China: evidences of changing source emissions, Sci. Total Environ., 545, 546–555, http://dx.doi.org/10.1016/j.scitotenv.2015.12.070, 2016.

Yan, C., Zheng, M., Sullivan, A., Bosch, C., Desyaterik., Andersson, A., Li, X., Guo, X., Zhou, T., Gustafsson, O., Collett Jr., J.: Chemical characteristics and light-absorbing property of water soluble organic carbon in Beijing: biomass burning contributions, Atmos. Environ., 121, 4-12, http://dx.doi.org/10.1016/j.atmosenv.2015.05.005, 2015.

Yang, M., Howell, S. G., Zhuang, J., and Huebert, B. J.: Attribution of aerosol light absorption to black carbon, brown carbon, and dust in China – interpretations of atmospheric measurements during EAST-AIRE, Atmos. Chem. Phys., 9, 2035–2050, https://doi.org/10.5194/acp-9-2035-2009, 2009.

Yao, X., Chan, C. K., Fang, M., Cadle, S., Chan, T., Mulawa, P., He, K., and Ye, B.: The water-soluble ionic composition of $PM_{2.5}$ in Shanghai and Beijing, China, Atmos. Environ., 36, 4223–4234, https://doi.org/10.1016/S1352-2310(02)00342-4, 2002.

Zhao, S., Tian, H., Luo, L., Liu, H., Wu, B., Liu, S., Bai, X., Liu, W., Liu, X., Wu, Y., Lin, S., Guo, Z., Lv, Y., and Xue, Y.: Temporal variation characteristics and source apportionment of metal elements in $PM_{2.5}$ in urban Beijing during 2018–2019, Environ. Pollut., 268, 115856, https://doi.org/10.1016/j.envpol.2020.115856, 2021.

779 Zhao, S., Tie, X., Cao, J., and Zhang, Q.: Impacts of mountains on black carbon aerosol under different synoptic meteorology
780 conditions in the Guanzhong region, China, Atmos. Res., 164–165, 286–296,
781 https://doi.org/10.1016/j.atmosres.2015.05.016, 2015

782 Zhao, S. P., Yu, Y., Yin, D., Yu, Z., Dong, L. X., Mao, Z., He, J. J., Yang, J., Li, P., and Qin, D. H.: Concentrations, optical
783 and radiative properties of carbonaceous aerosols over urban Lanzhou, a typical valley city: results from in-situ
784 observations and numerical model, Atmos. Environ., 213, 470–484, https://doi.org/10.1016/j.atmosenv.2019.06.046, 2019.

785 Zhang, Z., Gao, J., Engling, G., Tao, J., Chai, F., Zhang, L., Zhang, R., Sang, X., Chan, C., Lin, Z., and Cao, J.: Characteristics
786 and applications of size-segregated biomass burning tracers in China's Pearl River Delta region, Atmos. Environ., 102,
787 290–301. https://doi.org/10.1016/j.atmosenv.2014.12.009, 2015.

788 Zhang, J. P., Zhu, T., Zhang, Q. H., Li, C. C., Shu, H. L., Ying, Y., Dai, Z. P., Wang, X., Liu, X. Y., Liang, A. M., Shen, H.
789 X., and Yi, B. Q.: The impact of circulation patterns on regional transport pathways and air quality over Beijing and its
790 surroundings, Atmos. Chem. Phys., 12, 5031–5053, https://doi.org/10.5194/acp-12-5031-2012, 2012.

791 Zhang, Y., Li, M., Cheng, Y., Geng, G., Hong, C., Li, H., Li, X., Tong, D., Wu, N., Zhang, X., Zheng, B., Zheng, Y., Bo, Y.,
792 Su, H., and Zhang, Q.: Modeling the aging process of black carbon during atmospheric transport using a new approach: a
793 case study in Beijing, Atmos. Chem. Phys., 19, 9663–9680, https://doi.org/10.5194/acp-19-9663-2019, 2019.

794 Zhou, B., Wang, Q., Zhou, Q., Zhang, Z., Wang, G., Fang, N., Li, M., Cao, J.: Seasonal characteristics of black carbon aerosol
795 and its potential source regions in Baoji, China, Aerosol Air. Qual. Res., 18, 397–406, https://doi.org/
796 10.4209/aaqr.2017.02.0070, 2018.

797 Zotter, P., Herich, H., Gysel, M., El-Haddad, I., Zhang, Y., Močnik, G., Hüglin, C., Baltensperger, U., Szidat, S., and Prévôt,
798 A. S. H.: Evaluation of the absorption Ångström exponents for traffic and wood burning in the Aethalometer-based source
799 apportionment using radiocarbon measurements of ambient aerosol, Atmos. Chem. Phys., 17, 4229–4249,
800 https://doi.org/10.5194/acp-17-4229-2017, 2017

801

Table 1. The mass concentration of eBC from fossil fuel combustion (eBC_{fossil}) and eBC from biomass burning ($eBC_{biomass}$) associated with different clusters under four featured atmospheric motions

Motion category	Local scale dominance (LD) (40%)				Local scale strong and regional scale weak (LSRW) (17%)			
	L_{bj} = 70.9 km, S_{bj} = 107.8 km, R_{bj} = 0.35, R_{std} = 0.25				L_{bj} = 106.9 km, S_{bj} = 164.8 km, R_{bj}=0.33, R_{std} = 0.23			
	Cluster 1	Cluster 2	Cluster 3	Total average	Cluster 1	Cluster 2	Cluster 3	Total average
Trajectory percentage (%)	45	52	3	100	56	33	11	100
eBC_{fossil} (μg m^{-3})	$2.82^{a} \pm 1.59^{b}$	3.2 ± 1.73	3.64 ± 0.67	3.08 ± 2.07	2.42 ± 1.00	3.43 ± 1.17	2.89 ± 1.00	2.79 ± 1.73
$eBC_{biomass}$(μg m-^{3})	1.34 ± 1.07	1.72 ± 1.29	0.67 ± 0.87	1.52 ± 1.19	1.0 ± 0.85	1.17 ± 0.84	1.00 ± 0.64	1.06 ± 0.83

L_{bj}—resultant transport distance, S_{bj}—actual wind run distance at 100 m, R_{bj} —recirculation factor at 100 m, R_{std}—standard deviation for recirculation factor. a and b: Mean ± Standard deviation.

Table 1 (continued)

Motion category	Local scale weak and regional scale strong (LWRS) (14%)				Regional scale dominance (RD) (29%)			
	L_{bj} =159 km, S_{bj} = 183.4 km, R_{bj}=0.13, R_{std} = 0.20				L_{bj} =235.6 km, S_{bj} = 246.4 km, R_{bj}= 0.05, R_{std} = 0.18			
	Cluster 1	Cluster 2	Cluster 3	Total average	Cluster 1	Cluster 2	Cluster 3	Total average
Trajectory percentage (%)	42	22	36	100	41	20	39	100
eBC_{fossil} (μg m^{-3})	$1.32^{a} \pm 0.67^{b}$	2.02 ± 0.73	3.16 ± 1.19	2.15 ± 1.62	1.00 ± 0.64	1.02 ± 0.88	2.75 ± 1.26	1.69 ± 1.36
$eBC_{biomass}$(μg m-^{3})	0.67 ± 0.49	0.73 ± 0.47	1.19 ± 0.60	0.86 ± 0.58	0.64 ± 0.63	0.87 ± 0.69	1.26 ± 0.68	0.93 ± 0.72

L_{bj}—resultant transport distance, S_{bj}—actual wind run distance at 100 m, R_{bj} —recirculation factor at 100 m, R_{std}—standard deviation for recirculation factor. a and b: Mean ± Standard deviation.

Table 2. Direct radiative forcing efficiencies for equivalent black carbon (eBC) from fossil fuel combustion (eBC_{fossil}) and the eBC from biomass burning ($eBC_{biomass}$) under four atmospheric motion categories

Atmospheric motion category	$DRE_{eBCfossil, ATM}$ efficiency $((W\ m^{-2})/(\mu g\ m^{-3}))$	$DRE_{eBCbiomass, ATM}$ efficiency $((W\ m^{-2})/(\mu g\ m^{-3}))$
Local scale dominance (LD)	$10.2^{a} \pm 4.2^{b}$	10.3 ± 4.4
Local scale strong and regional scale weak (LSRW)	10.6 ± 5.7	10.2 ± 5.8
Local scale weak and regional scale strong (LWRS)	13.5 ± 6.7	14.7 ± 8.1
Regional scale dominance (RD)	15.6 ± 8.9	15.5 ± 8.4

a and b: Mean ± Standard deviation

Figure captions:

Figure 1. Four factors identified by source apportionment. Concentration (μg m^{-3}) of the chemical species and primary absorption coefficients (p_{abs}) (λ) at six wavelengths (λ = 370, 470, 520, 590, 660, or 880nm) (M m^{-1}) for each source are shown in grey. The blue square represents the contribution of each chemical species to the four different factors.

Figure 2. (a) Diel variations of the eBC from fossil fuel combustion (eBC_{fossil}) and (b) the eBC from biomass burning ($eBC_{biomass}$), (c) wind speed (m s^{-1}) and (d) planetary boundary layer height (m). The black bars of each hourly-averaged point show the standard deviation.

Figure 3. (a) The 75^{th} – 100^{th} percentile mass concentrations of the eBC from fossil fuel combustion (eBC_{fossil}) and (b) the eBC from biomass burning ($eBC_{biomass}$) under local scale dominance (LD, red circle), local scale strong and regional scale weak (LSRW, green circle), local scale weak regional scale strong (LWRS, purple circle) and regional scale dominance (RD, blue circle). S_{bj} is actual wind run distance at 100m height, R_{bj} is the recirculation factor, the grey area indicates good ventilation ($S_{bj} \geq 250$km, $R_{bj} \leq 0.2$), the yellow area indicates air stagnation ($S_{bj} \leq 130$km).

Figure 4. Mass concentrations of the eBC from fossil fuel combustion (eBC_{fossil}) and the eBC from biomass burning ($eBC_{biomass}$) during daytime (a, c) and nighttime (b, d) under local scale dominance (LD); local scale strong and regional scale weak (LSRW); local scale weak regional strong (LWRS); and regional scale dominance (RD).

Figure 5. Direct radiative effect (DRE) of the eBC from fossil fuel combustion (eBC_{fossil}) shaded in grey and the eBC from biomass burning ($eBC_{biomass}$) shaded in yellow (a) in the top atmosphere (TOA), surface (SUF), and the atmosphere atmospheric column (ATM) and (b) the $DRE_{eBC,ATM}$ of two types of eBC under local scale dominance (LD) shaded in light grey labeled as LD, local scale strong and regional scale weak (LSRW) shaded in light blue labeled as LSRW, local scale weak regional scale strong (LWRS) shaded in light grey labeled with LWRS and regional scale dominance (RD) shaded in light blue labeled as RD (c) DRE efficiencies of $eBC_{biomass}$ (shaded in yellow) and eBC_{fossil} (shaded by grey) in TOA, SUF and ATM (d) DRE efficiencies of $eBC_{biomass}$ and eBC_{fossil} at ATM under LD (shaded in light grey labeled as LD), LSRW (shaded in light blue labeled as LSRW), LWRS (shaded in light grey labeled as LWRS) and RD (shaded in light blue labeled with RD).

.

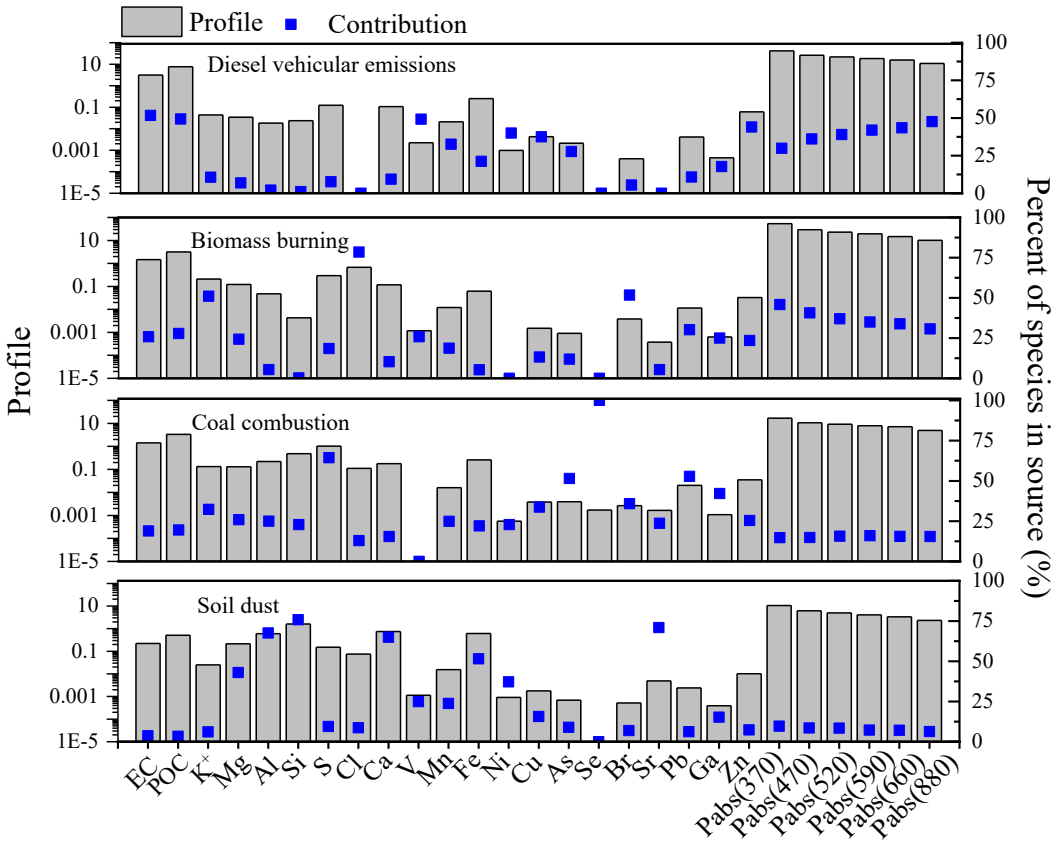

838

839 **Figure 1.** Four factors identified by source apportionment. Concentration (μg m^{-3}) of the chemical species and primary
840 absorption coefficients (p_{abs}) (λ) at six wavelengths (λ = 370, 470, 520, 590, 660, or 880nm) (M m^{-1}) for each source are shown
841 in grey. The blue square represents the contribution of each chemical species to the four different factors.

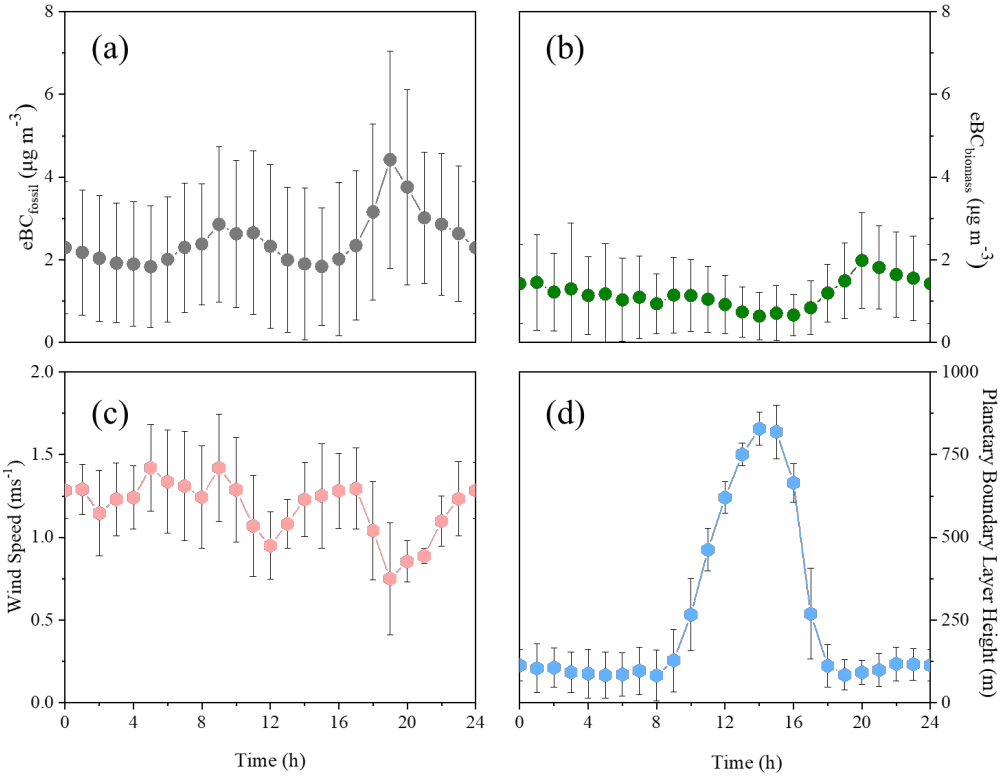

842

843 **Figure 2.** (a) Diel variations of the eBC from fossil fuel combustion (eBC_{fossil}) and (b) the eBC from biomass burning
844 ($eBC_{biomass}$), (c) wind speed (m s^{-1}) and (d) planetary boundary layer height (m). The black bars of each hourly-averaged point
845 show the standard deviation.

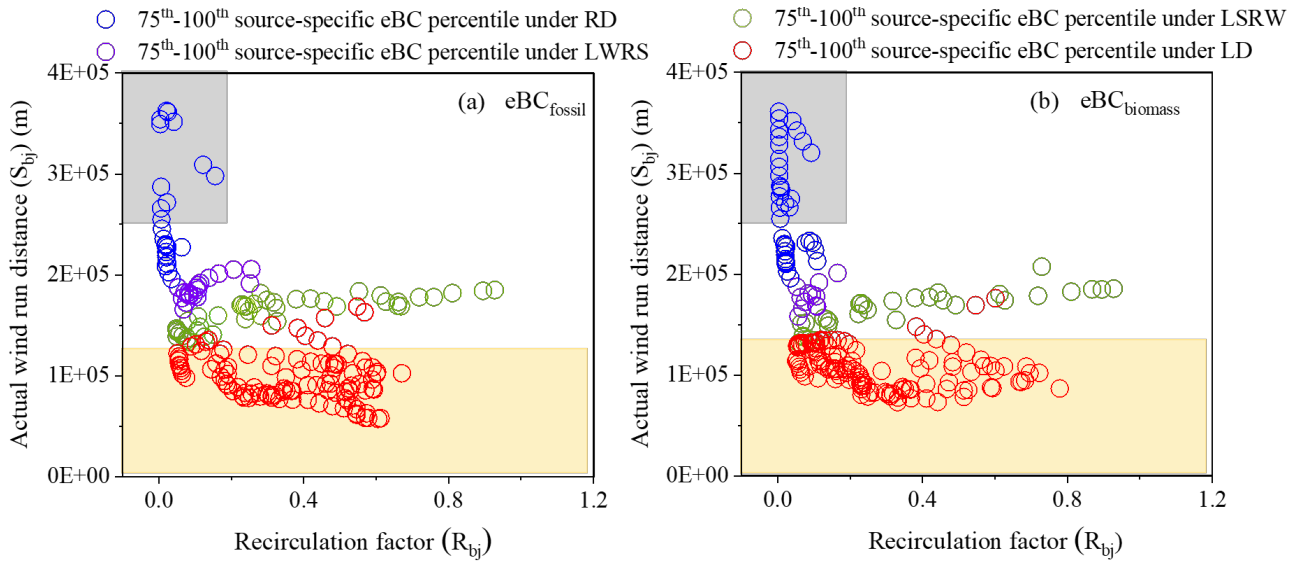

Figure 3. (a) The 75th – 100th percentile mass concentrations of the eBC from fossil fuel combustion (eBC_{fossil}) and (b) the eBC from biomass burning ($eBC_{biomass}$) under local scale dominance (LD, red circle), local scale strong and regional scale weak (LSRW, green circle), local scale weak regional scale strong (LWRS, purple circle) and regional scale dominance (RD, blue circle). S_{bj} is actual wind run distance at 100m height, R_{bj} is the recirculation factor, the grey area indicates good ventilation ($S_{bj} \geq 250$km, $R_{bj} \leq 0.2$), the yellow area indicates air stagnation ($S_{bj} \leq 130$km).

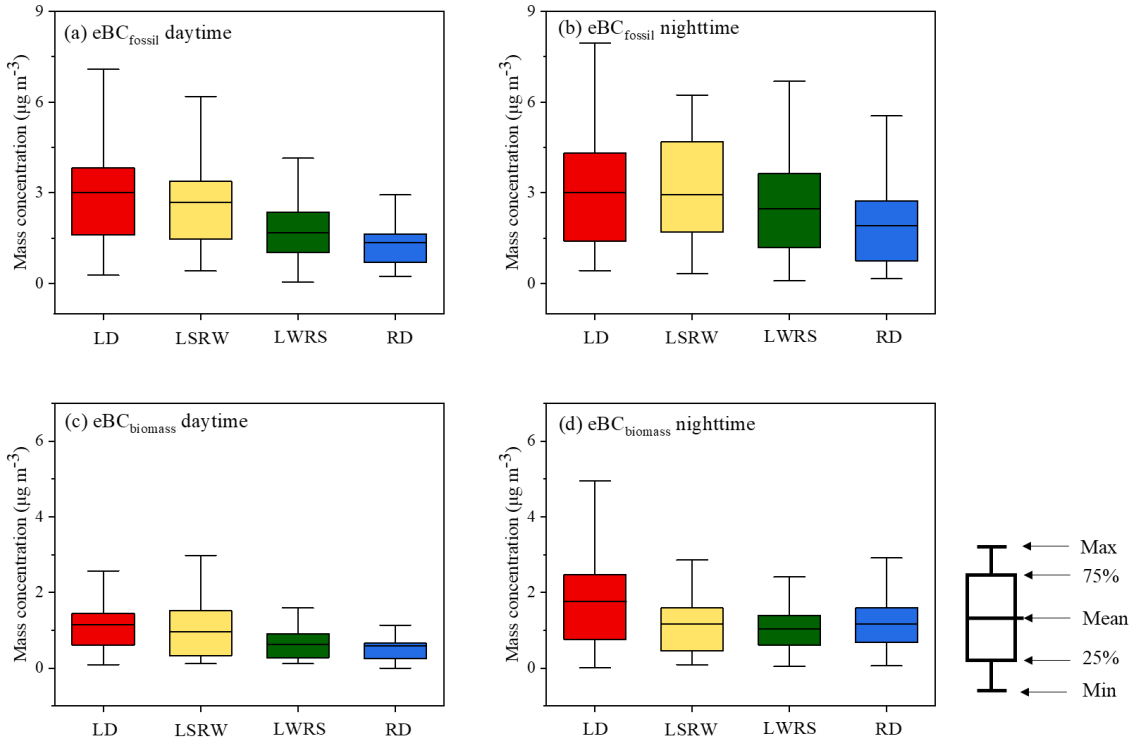

852

853 **Figure 4.** Mass concentrations of the eBC from fossil fuel combustion (eBC$_{fossil}$) and the eBC from biomass burning (eBC$_{biomass}$)
854 during daytime (a, c) and nighttime (b, d) under local scale dominance (LD); local scale strong and regional scale weak (LSRW);
855 local scale weak regional strong (LWRS); and regional scale dominance (RD).

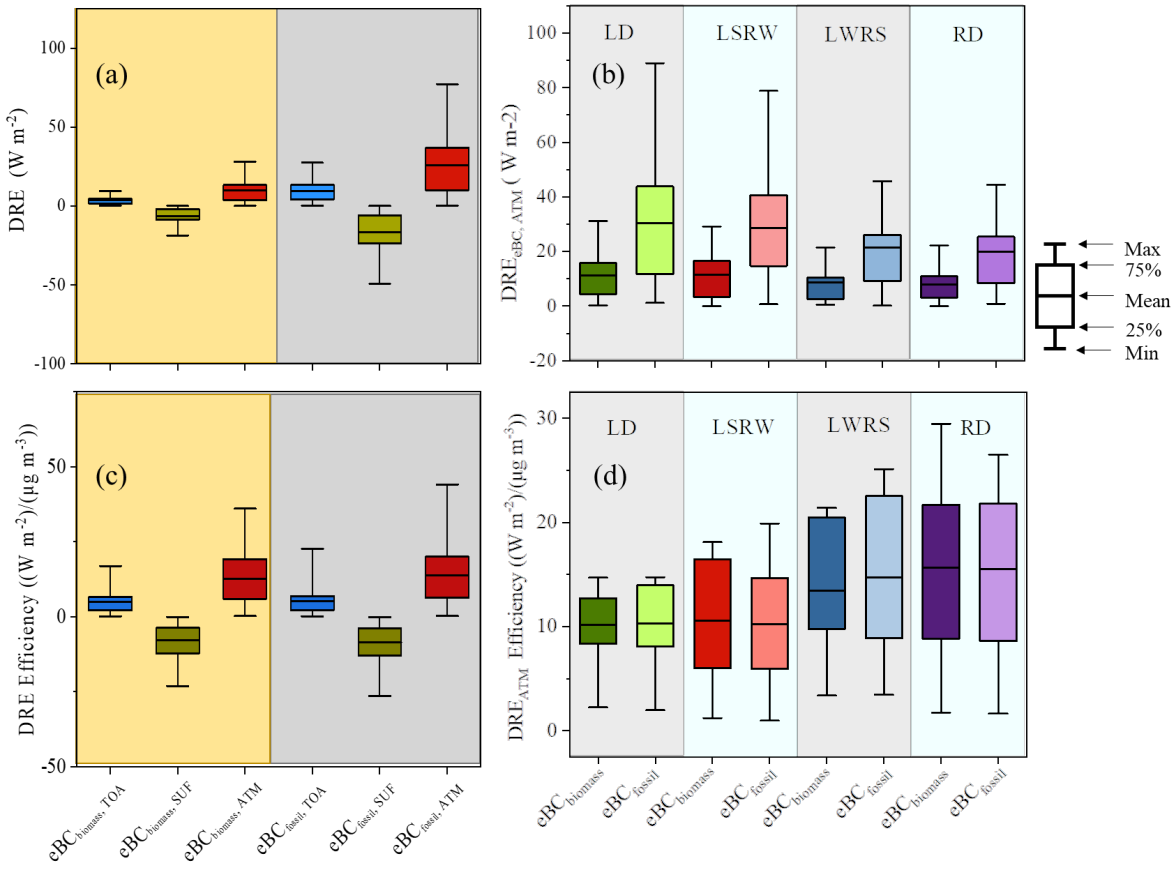

Figure 5. Direct radiative effect (DRE) of the eBC from fossil fuel combustion (eBC_{fossil}) shaded in grey and the eBC from biomass burning ($eBC_{biomass}$) shaded in yellow (a) in the top atmosphere (TOA), surface (SUF), and the atmosphere atmospheric column (ATM) and (b) the $DRE_{eBC,ATM}$ of two types of eBC under local scale dominance (LD) shaded in light grey labeled as LD, local scale strong and regional scale weak (LSRW) shaded in light blue labeled as LSRW, local scale weak regional scale strong (LWRS) shaded in light grey labeled with LWRS and regional scale dominance (RD) shaded in light blue labeled as RD (c) DRE efficiencies of $eBC_{biomass}$ (shaded in yellow) and eBC_{fossil} (shaded by grey) in TOA, SUF and ATM (d) DRE efficiencies of $eBC_{biomass}$ and eBC_{fossil} at ATM under LD (shaded in light grey labeled as LD), LSRW (shaded in light blue labeled as LSRW), LWRS (shaded in light grey labeled as LWRS) and RD (shaded in light blue labeled with RD).